



HAL
open science

Spectrophotometric Properties of 162173 Ryugu's Surface from the NIRS3 Opposition Observations

Deborah Domingue, Kohei Kitazato, Moe Matsuoka, Yasuhiro Yokota, Eri Tatsumi, Takahiro Iwata, Masanao Abe, Makiko Ohtake, Shuji Matsuura, Stefan Schröder, et al.

► **To cite this version:**

Deborah Domingue, Kohei Kitazato, Moe Matsuoka, Yasuhiro Yokota, Eri Tatsumi, et al.. Spectrophotometric Properties of 162173 Ryugu's Surface from the NIRS3 Opposition Observations. The Planetary Science Journal, 2021, 2, 10.3847/PSJ/ac14bb . insu-03713750

HAL Id: insu-03713750

<https://insu.hal.science/insu-03713750>

Submitted on 5 Jul 2022

HAL is a multi-disciplinary open access archive for the deposit and dissemination of scientific research documents, whether they are published or not. The documents may come from teaching and research institutions in France or abroad, or from public or private research centers.

L'archive ouverte pluridisciplinaire **HAL**, est destinée au dépôt et à la diffusion de documents scientifiques de niveau recherche, publiés ou non, émanant des établissements d'enseignement et de recherche français ou étrangers, des laboratoires publics ou privés.



Distributed under a Creative Commons Attribution 4.0 International License



Spectrophotometric Properties of 162173 Ryugu's Surface from the NIRS3 Opposition Observations

Deborah Domingue¹ , Kohei Kitazato², Moe Matsuoka³ , Yasuhiro Yokota³ , Eri Tatsumi^{4,5,6} , Takahiro Iwata³, Masanao Abe³ , Makiko Ohtake³, Shuji Matsuura⁷ , Stefan Schröder⁸ , Faith Vilas¹ , Antonella Barucci⁹, Rosario Brunetto¹⁰ , Driss Takir¹¹, Lucille Le Corre¹ , and Nicholas Moskovitz¹²

¹ Planetary Science Institute, Tucson AZ, USA

² University of Aizu, Fukushima, Japan

³ Institute of Space and Astronautical Science, Japan Aerospace Exploration Agency, Japan

⁴ Instituto de Astrofísica de Canarias, Tenerife, Spain

⁵ Department of Astrophysics, University of La Laguna, Tenerife, Spain

⁶ Department of Earth and Planetary Science, University of Tokyo, Tokyo, Japan

⁷ Kwansai Gakuin University, Nishinomiya, Japan

⁸ Deutsches Zentrum für Luft- und Raumfahrt (DLR), Berlin, Germany

⁹ LESIA, Observatoire de Paris, Université PSL, CNRS, Univ. de Paris, Sorbonne Université, France

¹⁰ Institut d'Astrophysique Spatiale, Université Paris-Saclay, CNRS, 91400 Orsay, Orsay, France

¹¹ Jacobs/NASA Johnson Space Center, Houston, TX, USA

¹² Lowell Observatory, Flagstaff, AZ, USA

Received 2020 October 17; revised 2021 June 14; accepted 2021 June 18; published 2021 September 1

Abstract

Examination of the opposition geometry properties show that Ryugu's surface regolith is commensurate with laboratory studies of the photometric behavior of powdered carbonaceous chondrites. The regolith is consistent with a broad grain size distribution that contains a fine-grained component.

Unified Astronomy Thesaurus concepts: Asteroids (72); Surface photometry (1670); Spectroscopy (1558)

1. Introduction

Hayabusa2, the Japanese Aerospace Exploration Agency's (JAXA) spacecraft for the asteroid sample return mission to the near-Earth asteroid 162173 Ryugu, began conducting remote-sensing observations in June 2018. Among the observations were near-infrared (1.8–3.2 μm) reflectance measurements acquired by the Near-Infrared Spectrometer (NIRS3). Examinations of the spectral observations acquired by NIRS3 show a dark, compositionally homogeneous rubble-pile object with a weak, narrow absorption feature centered at 2.72 μm (Kitazato et al. 2019). This feature is attributed to hydroxyl (OH)-bearing minerals that are ubiquitously present across the entire observed surface (Kitazato et al. 2019). Clustering analyses of the NIRS3 data indicate slight differences in the content of the hydrated materials along with regolith grain size variations (Barucci et al. 2019). Photometric analyses of the equatorial and southern midlatitudes using Hapke's model show that while, to first order, the single-scattering albedo properties are homogeneous, there are localized brighter and darker regions (Pilorget et al. 2021). The darker regions tend to be associated with a slightly deeper 2.72 μm feature, which Pilorget et al. (2021) ascribe to enrichment of dark fines coupled to hydrated phases.

In this study we present an examination of the opposition observations acquired by the NIRS3 instrument to gain further insight into the structural properties of Ryugu's regolith. This study examines the effects of footprint resolution, spectral variability across the surface, and variations as a function of wavelength within this opposition data set. The goal is to gain

an understanding of the nature and magnitude of the surface spectral variations, the global photometric properties, and their combined implications for the regolith on Ryugu. The opposition observations provide insight into the nature and properties of Ryugu's surface under unique observing conditions. This study begins with a presentation of the spectral characteristics of Ryugu's opposition data set followed by the examination and modeling of the photometric properties of this data set. Both spectral and photometric properties are compared with similar examinations from the Optical Navigation Camera (ONC) imaging data set, and the results are placed in context with other small bodies studied in our solar system.

2. The Data Set

The NIRS3 is a point spectrometer with a 0.1° field of view, which obtained continuous point-target spectra over Ryugu's surface. The observations used in this study are a subset of those made over the entire mission and acquired by the NIRS3 prior to the first touchdown (TD1) for sample collection in 2019 February. This study focuses on the infrared spectra of Ryugu acquired under opposition (phase angles, α , $< 5^\circ$) and near opposition ($\alpha < 30^\circ$) geometries at various spatial scales over the near-equatorial, low-latitude regions (Figure 1).

For this study, all observations acquired prior to TD1 were binned according to footprint resolution in consecutive bins of 2 m, beginning with the first bin of 4–6 m footprint size. This resolution range (2 m) was chosen as the smallest resolution with sufficient data to cover the incidence, emission, and phase angle space for modeling. All data for which geometric information (latitude, longitude, altitude, incidence, emission, and phase angle) was available were examined for this analysis. Each bin was examined for phase angle coverage. Only four footprint size bins contained opposition observations: bin 4–6 m, bin 6–8 m, bin 8–10 m, and bin 38–40 m. These four bins were used for this

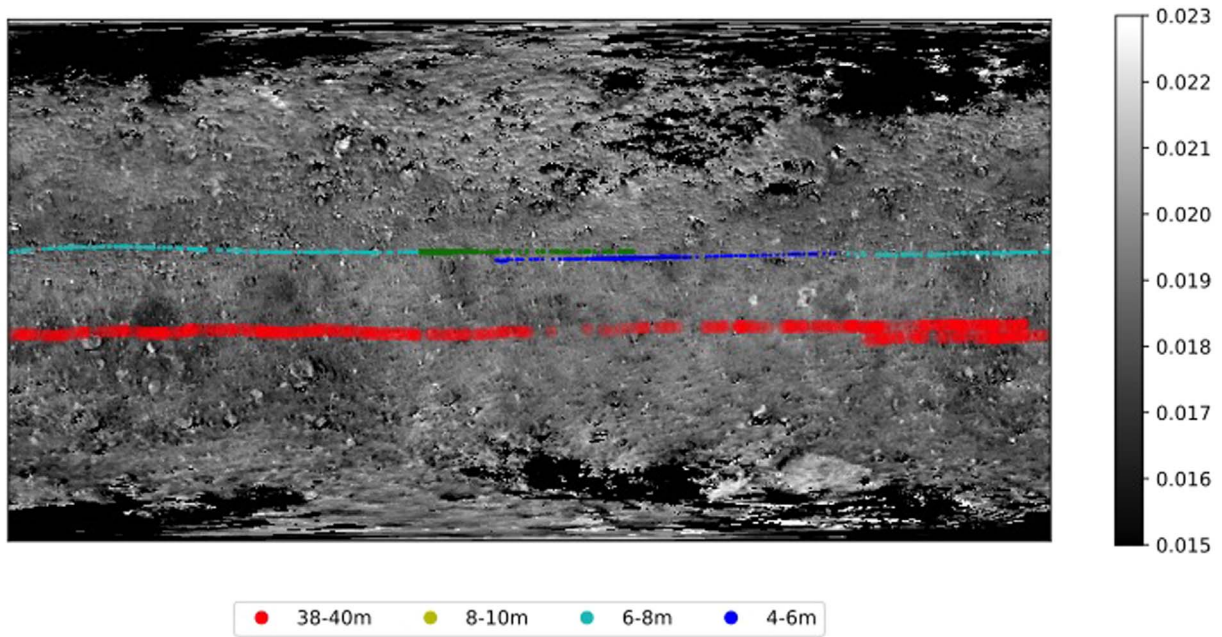


Figure 1. NIRS3 footprints of the opposition observations used in this study overlaid on the ONC-T v -band standardized reflectance map (Tatsumi et al. 2020). The circles are sized to the footprint resolution of the spectra with blue representing 4–6 m resolution, cyan representing 6–8 m resolution, yellow representing 8–10 m resolution, and red representing 38–40 m resolution.

study of the opposition surge. All data within each footprint size bin, regardless of phase angle value, were used for the study.

Each spectrum ranges in wavelength from 1.8 to 3.2 μm (Iwata et al. 2017). This analysis focuses on the 76 channels ranging in wavelength from 1.801 to 3.149 μm . This wavelength range was selected because those channels above 3.149 μm are affected by thermal emission and those channels below 1.8 μm are within the wavelength region where the NIRS3 detector sensitivity decreases (Iwata et al. 2017; Kitazato et al. 2019). The observations were converted to reflectance using the calibration algorithm described in Iwata et al. (2017).

The data within each footprint size bin were organized into photometric angular groups. The groups were defined by every 1° of incidence and emission angle and every 0.1° of phase angle for observations acquired in the opposition region ($\alpha < 5^\circ$). This binning was performed to provide uniform data coverage within the photometric angle space available, yet provide the angular resolution within the opposition surge to constrain the modeling parameters. Groups outside the opposition region were defined by every 1° of incidence and emission angle and every 1° of phase angle. A representative spectrum for each angular group was selected at random. This method was selected to keep angle values connected to actual reflectance values. These representative spectra from each angular group, along with their photometric angle values, comprised the data set that was modeled. The modeling effort is described in Section 3. The results are examined both as a function of footprint size and as a combined, collective group.

A summary of the general spectral and photometric characteristics of the data set include:

1. The smaller footprint resolution bins (< 10 m) represent terrains north of the equatorial ridge while the largest footprint resolution bin (38–40 m) represents terrains south of the equatorial ridge (Figure 1).
2. The footprints within each footprint resolution bin fall on different albedo terrains (Figure 1).

3. The angular groups display some variability ($\sim 10\%$) within the spectra contained in that group, independent of the footprint resolution bin (Figure 2).
4. Spectral properties are uniform between different footprint bins (Figure 3).
5. The phase curve in the opposition region displays both wavelength and footprint resolution bin related variations (Figure 4).
6. The phase curve at larger phase angles ($\alpha > 10^\circ$) shows no variations with footprint resolution bin, but wavelength-dependent variations are observed at a few phase angles $> 16^\circ$, which may be a consequence of the incidence and emission angle coverage (Figure 4).

2.1. Spectral Properties of the Data Set

The NIRS3 spectra in the 1.8–3.2 μm range show a fairly flat spectrum with a sharp absorption feature at ~ 2.72 μm , indicative of the presence of hydroxyl (OH)-bearing minerals (Kitazato et al. 2019). These spectral characteristics are ubiquitous over the surface (Kitazato et al. 2019); however, variations in overall albedo and depth of the 2.72 μm feature across the surface are observed (Barucci et al. 2019).

Many angular bins do not contain any data. Those angular bins that are present in the data set contain a small number of spectra (Figure 2 displays an example for the 6–8 m footprint group of spectra acquired within angular bins $4^\circ < i < 5^\circ$, $8^\circ < e < 9^\circ$, and $12^\circ < \alpha < 13^\circ$). Spectral variability is predominantly in albedo, not in spectral slope or the absence/presence of spectral features (Figure 3). This is attributed to local differences in Ryugu’s surface and is discussed in more detail in Section 2.2. The small variations observed in the spectra are the result of calibration residuals and not Gaussian photon noise (Iwata et al. 2017).

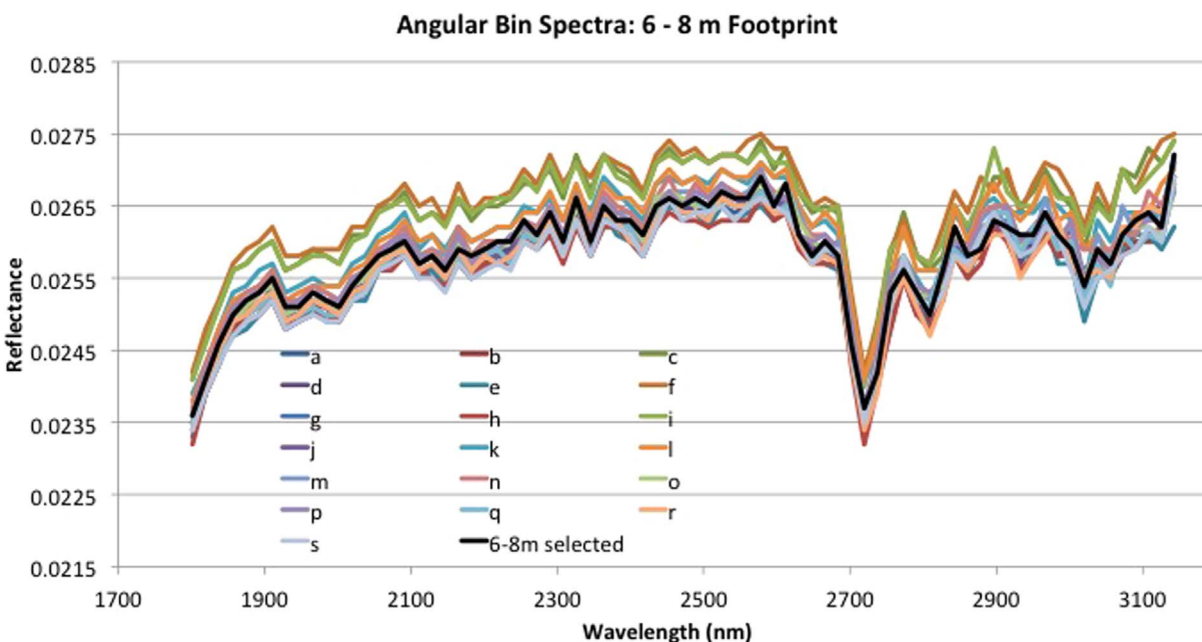


Figure 2. The spectra shown are from the angular bin with incidence angle of 4° – 5° , emission angle of 8° – 9° , and phase angle of 12° – 13° from the 6–8 m footprint resolution group. All spectra from this angular bin and footprint resolution group (labeled alphabetically) are displayed. The representative spectrum for this angular bin and footprint resolution group is shown as a solid black line. The small variations are due to calibration residuals.

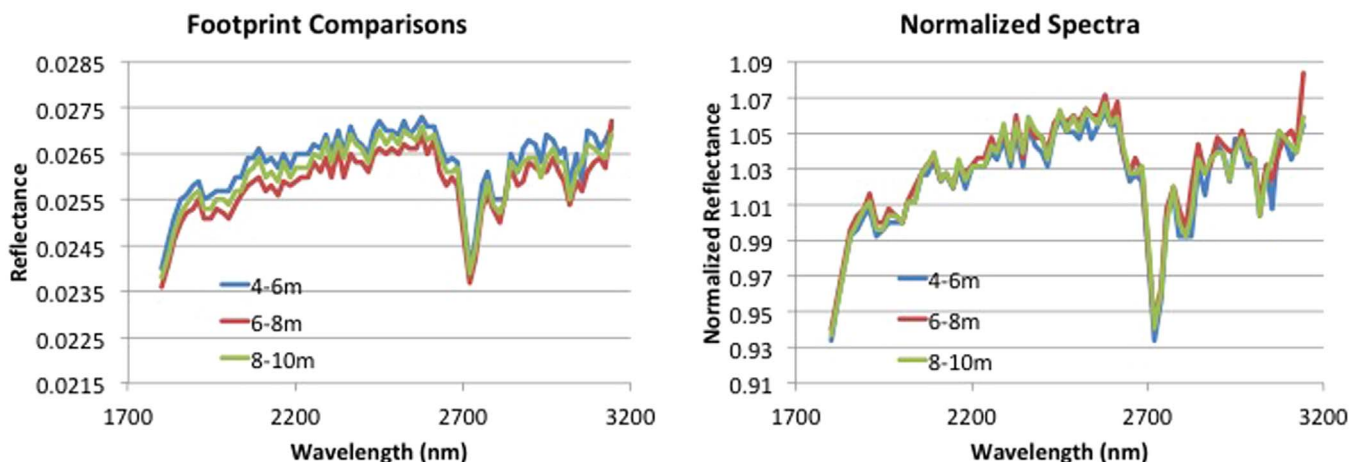


Figure 3. Representative spectra from the angular bin with incidence angle of 4° – 5° , emission angle of 8° – 9° , and phase angle of 12° – 13° from the three footprint resolution groups that contain spectra within this angular range. The spectra are shown absolute reflectance (left) and normalized to unity at $\sim 2 \mu\text{m}$ (right).

2.2. Photometric Characteristics of the Data Set

Another method for examining the spectral data is to look at the variations in reflectance as a function of phase angle with respect to wavelength. Comparisons of the phase curve (reflectance versus phase angle) at various wavelengths show that the NIRS3 phase curve varies with wavelength, most notably within the opposition region (Figure 4). Examination of the phase curve at 2, 2.56, and $2.7 \mu\text{m}$ (Figure 4) shows that for each illumination and viewing geometry, the reflectance as a function of phase angle is wavelength dependent and possibly dependent on footprint resolution.

The variation with wavelength in the phase curve behavior follows the variation with albedo. The intriguing variation occurs at the opposition phase angles and is a function of footprint size. The incidence and emission angle variation within the different footprints is similar within each footprint

size's data set. The largest footprint data set (38–40 m) breaks the smooth trend in reflectance with the phase angle seen between the other footprint size data sets. These footprints in the 38–40 m data set all fall in the southern hemisphere of Ryugu, between $\sim -20^{\circ}$ and -15° latitude, whereas the footprints for the other data sets lie in the northern hemisphere, closer to the equatorial ridge between $\sim 5^{\circ}$ and 12° latitude (Figure 1). The variations in the opposition region suggest potential differences between the southern latitudes and the north, near-equatorial region. Because the phase variations between the different footprint size data sets are not apparent in the larger phase angles, this suggests the differences are due to structural variations that would affect the opposition region greatest, which include porosity/compaction and grain size. While the focus of this study is the global spectrophotometric properties of Ryugu's surface, it is important to note the indicators of potential regional variations.

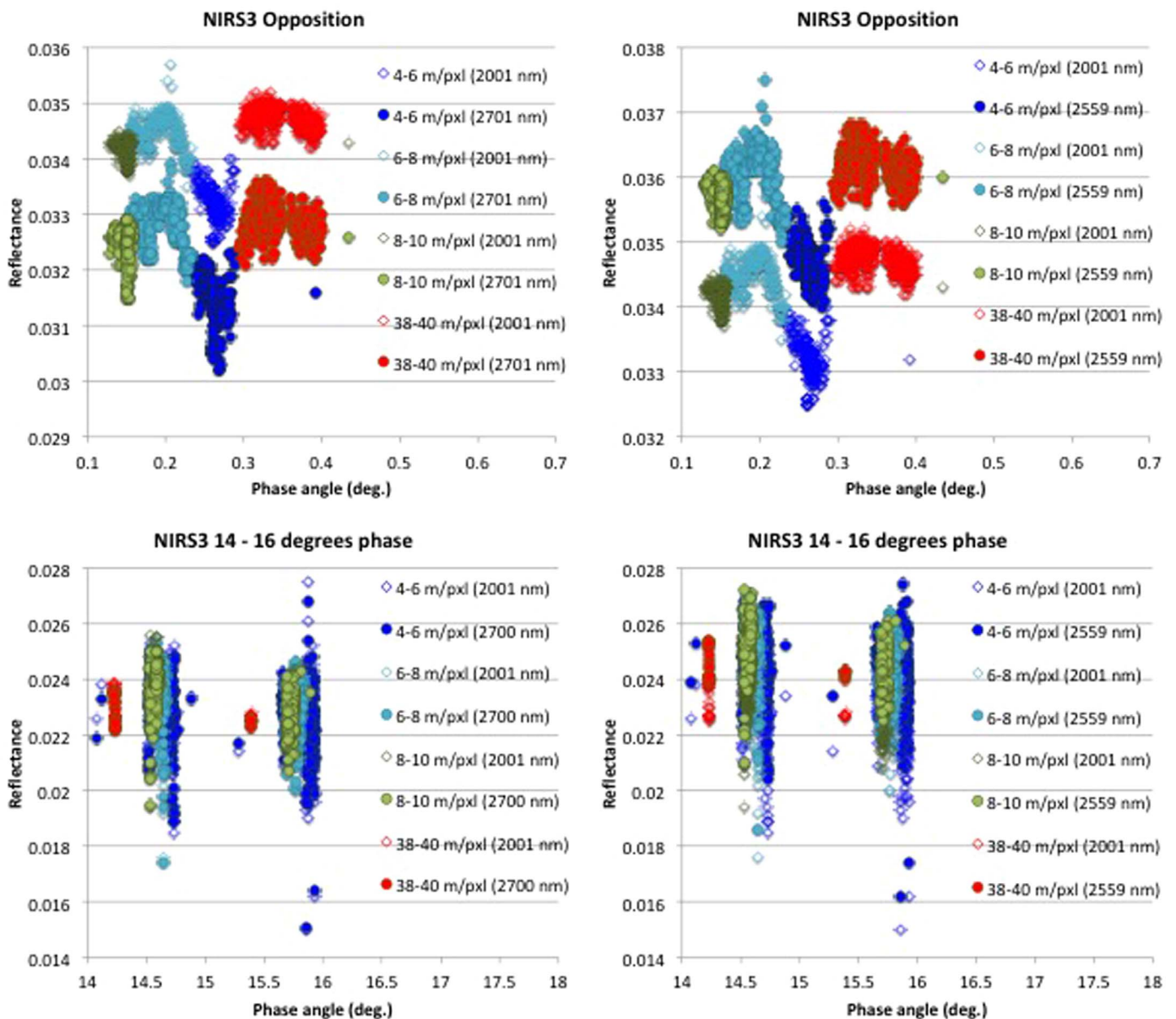


Figure 4. Different regions within the NIRS3 phase curve are shown comparing three different wavelengths and all four footprint resolution groups. The size groups are represented by the same colors as in Figure 1. The left column compares the phase curve at $2\ \mu\text{m}$ (open diamonds) and $2.7\ \mu\text{m}$ (solid circles). The right column compares the phase curve at $2\ \mu\text{m}$ (open diamonds) and $2.559\ \mu\text{m}$ (solid circles). The top row displays the opposition region, and the bottom row displays the 14° – 15° phase range. There are wavelength-dependent differences seen at the opposition phase angles that are not present at the higher phase angles.

3. Model and Modeling Methodology

The data sets from each footprint resolution bin were combined to form a data set for modeling the opposition region of Ryugu’s phase curve. The data range in phase angle from 0.128° to 28.141° . The incidence and emission angle coverage is shown in Figure 5. Here we describe the controlling mechanisms for the opposition surge, the model formulation, and the approach taken with the model application.

The surge in brightness near opposition is a characteristic of particulate media (e.g., Hapke 2012), though disk-integrated observations of several dark objects do not show this increase in brightness at small ($<1^\circ$) phase (e.g., Schevchenko et al. 2008). The cause for the lack of a detectable opposition surge may be due to the lack of a fine (micrometer scale) to moderate (millimeter scale) grained component, a highly absorbing

composition, or a combination of the two. Its amplitude and width are a function of a variety of physical characteristics, including composition, grain size and shape, and porosity (e.g., Hapke 2012). When examining or extrapolating regolith characteristics from spectral observations and photometric modeling results, it is important to note that the portion of the regolith that is under scrutiny is the optically active portion. This is the top layer of the regolith that interacts with the incident and subsequently reflected light. The depth within the regolith this corresponds to is dependent on the opacity and scattering efficiencies of the regolith materials, but for visible and near-infrared wavelengths this typically corresponds to the upper hundreds of micrometers. Given Ryugu’s highly absorbing regolith (it is among one of the darkest objects observed, with a physical albedo of $\sim 3.5\%$ at $2.0\ \mu\text{m}$ as calculated from our modeling results below), sunlight will not penetrate beyond a

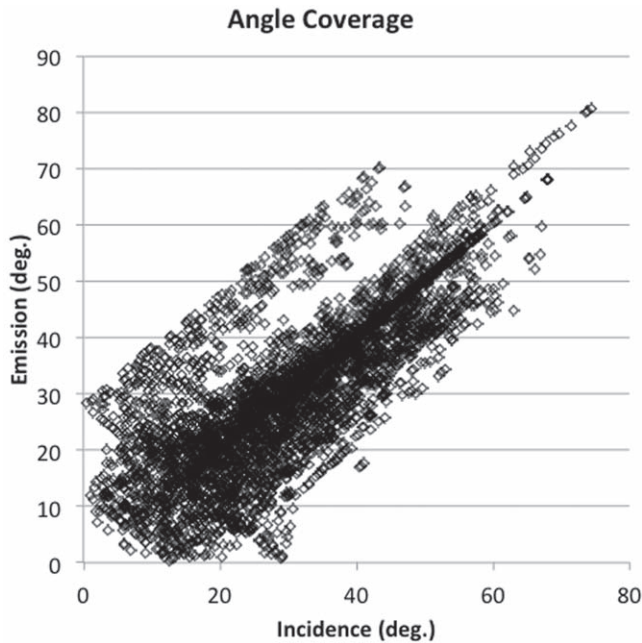


Figure 5. This graph displays the coverage in incidence (i) and emission angle (e) of the opposition data set examined in this study.

few tens of wavelengths. Within absorption features, such as the $2.72 \mu\text{m}$ band, the absorption coefficient increases and this can significantly reduce the penetration depth of incident photons. This section of the regolith that interacts with the incident sunlight is the portion of the regolith we can characterize using photometric modeling. We cannot state what the properties of the regolith are at depths below a few tens of micrometers, based solely on photometric behavior.

The first step for understanding the opposition observations is to understand the mechanisms that produce this surge in brightness at phase angles smaller than 5° . A concise description of these mechanisms is given in Schröder et al. (2018) and is summarized here. The two dominant mechanisms contributing to the opposition effect are shadow hiding (SHOE) and coherent backscatter (CBOE). SHOE occurs when the illumination source (the Sun) is directly behind the detector/observer (in this case the spacecraft) and areas that would be in shadow are now illuminated. The resulting effect is to increase the reflectance from the surface (Hapke 1984, 1986; Shkuratov et al. 1994; Shkuratov & Helfenstein 2001). CBOE occurs through the constructive interference of light at very small phase angles (Mishchenko & Dlugach 1993; Mishchenko et al. 2009; Dlugach & Mishchenko 2013), and in order to be observed, regolith grains with sizes on the order of the wavelength (in this case approximately $1\text{--}4 \mu\text{m}$) are required (Mishchenko & Dlugach 1993; Schröder et al. 2018). Coherent backscatter contributes to the opposition surge for atmosphereless bright bodies; however, this contribution is considered negligible for dark objects (Shevchenko & Belskaya 2010; Shevchenko et al. 2012). For example, Markkanen et al. (2018) argue for the possible existence of coherent backscatter in the opposition observations of comet 67P/Churyumov–Gerasimenko, whose albedo is very dark (0.059 at 550 nm, Sierks et al. 2015; and 0.065 at 649 nm, Fornasier et al. 2015, Hasselmann et al. 2017). However, the increase at opposition that they attribute to coherent backscatter is at a $\sim 10\%$ level, making its contribution very small. Ryugu reflects $\sim 2\%$ of the incident sunlight, thus

multiple scattering is a small contribution to the reflected light from such an absorbing surface and its contribution to a coherent backscatter opposition will also be very small. In the absence of polarization measurements, the photometric observations alone may not be diagnostic of coherent backscatter. The phase angle coverage for the Ryugu observations is very limited ($<30^\circ$ phase), thus models with numerous (8+) parameters will not be well constrained. In the modeling presented here, we consider only a shadow-hiding component to the opposition effect and a single-term particle-scattering function to describe the data set.

Several photometric models, and variations on these models, have been used to study reflectance from planetary surfaces as a function of illumination and viewing geometry. One of the most common models currently in use is that derived by Hapke (1981, 1984, 1986, 1993, 2002, 2008, 2012), which is based on geometric optics and the equations of radiative transfer. It incorporates expressions and parameters to account for surface roughness, grain size and compaction, and grain-scattering properties. The parameters in this model are derived to correlate to specific surface properties or sets of properties. However, many of these derivations have built-in assumptions regarding the scattering surface. Laboratory tests of the correlation between Hapke model parameters with sample characteristics have shown evidence that the Hapke model parameters can be qualitatively related to physical properties (Shepard & Helfenstein 2007; Helfenstein & Shepard 2011; Souchon et al. 2011; Kaydash et al. 2012) and that the parameter values are often influenced by more than one property (Shepard & Helfenstein 2007). A quantitative correlation with regolith properties has yet to be firmly established in the laboratory. This study applies the Hapke model to the NIRS3 spectrophotometric data set as this model has been applied to numerous solar system objects. The interpretations of the results provide a qualitative understanding of planetary regoliths and a mechanism to compare to similarly studied objects using a model based on physical properties.

3.1. The Model

The model used to analyze the NIRS3 data set is that described by the Hapke set of equations for expressing disk-resolved reflectance, $(I/F)_R$, which is given by

$$(I/F)_R = \frac{w}{4} \frac{\mu_{0e}}{\mu_{0e} + \mu_e} \{ [P(\alpha)[1 + B(\alpha)] + [H(\mu_{0e})H(\mu_e) - 1] \} S(i, e, \alpha, \bar{\theta}), \quad (1)$$

where w is the single-scattering albedo, $P(\alpha)$ is the single-particle scattering function (Equation (2)), and B is the opposition term (Equation (3)). For this study a single-term Henyey–Greenstein function was chosen for $P(\alpha)$, such that

$$P(\alpha) = \frac{(1 - b^2)}{[1 - 2b \cos(\alpha) + b^2]^{3/2}}, \quad (2)$$

where b describes the amplitude of the scattering peaks. Positive values of b correspond to backward scattering and negative values to forward scattering. A single-term phase function is used because the data set does not capture the forward-scattering direction ($\alpha > 110^\circ$) and only contains observations with phase angle values below 30° .

The opposition term, $B(\alpha)$, in this expression is given by

$$B(\alpha) = \frac{B_{S0}}{1 + \frac{\tan(\alpha/2)}{h_s}}, \quad (3)$$

where B_{S0} describes the amplitude of the opposition surge and h_s describes the width of the opposition peak. This expression assumes that the shadow-hiding mechanism (SHOE) is the sole contributor to the opposition effect. This assumption is made because Ryugu's albedo is extremely low; it is one of the darkest objects to be visited by a spacecraft.

In the disk-resolved reflectance equation (Equation (1)) the surface roughness term, $S(i, e, \alpha, \theta)$, accounts for the large-scale roughness, and μ_{oe} and μ_e are the modified cosines of the incident and emission angles, respectively, due to surface roughness. The surface roughness is defined as the average surface tilt on the size scale ranging from a few particle diameters to the resolution of the detector footprint (e.g., Hapke 2012). The $H(x)$ terms in the reflectance equation are the Chandrasekhar H functions. The mathematical expressions for these terms and their derivation can be found in Hapke (1981, 1984, 1986, 1993, 2002, 2008, 2012).

3.2. Inversion Modeling Technique

The modeling methodology used was a least-squares grid search that minimized the value of eta (η), defined by

$$\eta = \sum_{i=1}^N \sqrt{(r_{\text{measured}} - r_{\text{model}})^2} / N, \quad (4)$$

where N is the number of measurements, r_{measured} is the NIRS3 measured reflectance, and r_{model} is the calculated reflectance using the Hapke model. This assumes that the errors in the measured reflectance are the same for each measurement within a single wavelength. Wavelength-dependent variations in η are a result of both different wavelength-to-wavelength standard deviation differences in the observations and spectral dispersion (reflectance variability of the surface) within the different wavelength data sets. The grid search was defined by a range and increment (grid size) for each parameter, and all combinations across the parameter values were examined. All parameters were varied simultaneously, and the top 10 parameter sets that resulted in the lowest values of η were recorded. This is the same methodology used by Domingue et al. (2016a, 2016b, 2018). Each wavelength channel was modeled independently. The independent modeling of each wavelength channel does not constrain the model parameter values to be a smooth function of wavelength. The wavelength-to-wavelength variability in the parameter values will reflect a combination of the difference standard deviations in reflectance at each wavelength, due to both reflectance variations from sampling different areas on the surface and channel-to-channel differences in the instrument response.

The initial grid size for w was 0.005, B_o was 0.05, h and b were 0.01, and $\bar{\theta}$ was 5° . The final grid size was 0.001 for w , 0.005 for B_o , 0.001 for h and b , and 1° for $\bar{\theta}$. The final grid size chosen for each parameter reflects the level to which the parameter can be determined given the variations in the data set at each wavelength. Tests of finer grid increments showed no significant ($\lesssim 0.2\%$) differences in η values, indicating that the data does not have sufficient precision to determine more

refined model parameter values. The range in values for each parameter depended on the model run because the data were modeled in a stepwise fashion. In the initial modeling run, where a run is where all the wavelengths have been modeled using the same parameter constraints, the only constraint was placed on the opposition amplitude parameter, B_o . In this initial run, B_o was constrained to be less than unity. This is in line with Ryugu's surface being dark and the dominant mechanism for producing the opposition surge is shadow-hiding. The parameter ranges for the initial run were 0.03–0.06 for w , 0–1 for B_o , 0.001–0.171 for h , 0.20–0.55 for b , and 10–35 for $\bar{\theta}$. These ranges were based on the model values obtained by Tatsumi et al. (2020) for the Telescopic Optical Navigation Camera (ONC-T) modeling efforts.

Prior to the second step, the values of the surface roughness parameter and the single-particle scattering function parameter were examined. The median value of the surface roughness parameter, $\bar{\theta}$, across all wavelengths, was found to be 29° with a range of values between 28° – 31° over all wavelengths. Thus, for the second run, the value of $\bar{\theta}$ was constrained to be 29° . In the derivation of the Hapke model equations, the value of $\bar{\theta}$ is defined to be wavelength independent, thus constraining the value of $\bar{\theta}$ to 29° across all wavelengths is in line with the definition of this parameter.

The phase angle coverage in this data set only samples the backward-scattering direction, thus this study utilized only a single-term Henyey–Greenstein single-particle scattering function (Equation (2)) for $P(\alpha)$. However, there is a mathematical coupling in the Hapke equations between w , $P(\alpha)$, and $\bar{\theta}$, especially over this small phase angle range (i.e., Hapke 2012). Using the median value of $\bar{\theta}$ across all wavelengths not only aligns with the parameter's derivation and definition but also assists in decoupling the values of these three parameters. In addition, the value of $P(\alpha)$ also affects the opposition terms over this phase angle range dominated by the opposition region. The values of w , B_o , h , and b after the initial run all displayed strong wavelength variations, especially between 2.4 and $3.0 \mu\text{m}$. In order to minimize the mathematical coupling between these parameters as the source of these wavelength dependencies, the value of the single-particle scattering function parameter, b , was set to the median value over wavelengths from 1.8 to $2.4 \mu\text{m}$. The median value of b , in this wavelength range, is 0.318 and is representative of a narrow range of values from 0.315 to 0.324. Over the small range of phase angles available in this data set, the single-particle scattering function is not well constrained. The narrow range of values for b produces small fluctuations in the single-particle scattering function that can be compensated for by small changes in w , θ , or a combination of the two. Thus, constraining b and θ to be uniform in wavelength provides a method to characterize the wavelength dependencies in the opposition parameters.

In the second, and final run, the parameters w , B_o , and h were varied while the value of b was set to 0.318 and the value of $\bar{\theta}$ was set to 29° . The grid size was 0.001, 0.005, and 0.001 for w , B_o , and h , respectively. The parameter value ranges were 0.04–0.06, 0.3–1, and 0.01–0.21 for w , B_o , and h , respectively. This range of values was based on the range of values from the top 10 solutions from the initial run. The final parameter values, as a function of wavelength, are displayed in Figure 6. The error bars, E , for each parameter were calculated based on the grid size of the final run and the range of values within the top

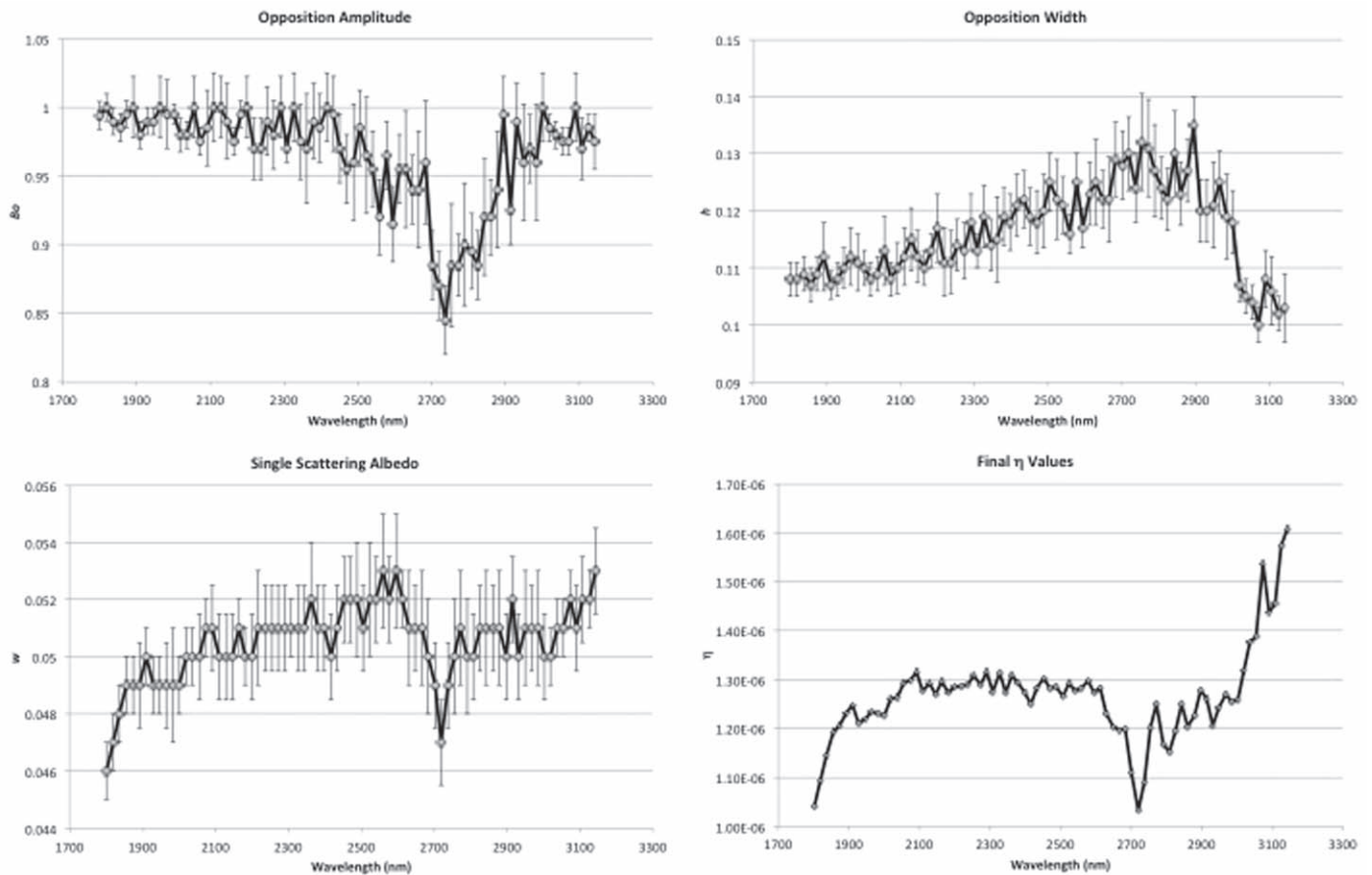


Figure 6. The final Hapke parameter values, as a function of wavelength, show that the wavelength variation in the single-scattering albedo is similar to that seen in the reflectance spectra. The sharp absorption at 2700 nm is apparent in both reflectance and the single-scattering albedo. The wavelength variations in the opposition parameters are broader. The η values, which mark the goodness of fit, are also wavelength dependent, indicating potential thermal contributions may still remain in the data set beyond 3000 nm. The displayed error is $\pm E$.

10 solutions such that

$$E = \text{inc} + (p_{\max} - p_{\min})/2,$$

where inc is the final grid size, and p_{\max} and p_{\min} are the maximum and minimum parameter values within the top 10 solutions. The value of the parameters cannot be discerned at a finer resolution than the grid size, thus the minimum error value is equivalent to the grid size (inc). The parameter value with error bars for the single-particle scattering function amplitude, b , is $0.318^{+0.007}_{-0.004}$. The parameter value with error bars for the surface roughness parameter, $\bar{\theta}$, is $29^{\circ} \pm 3_{-2}$. These error bars were calculated in the same manner, using the final grid size from the first run.

4. Modeling Results

Examination of the parameter values in Figure 6 shows that they are not a smooth function of wavelength (they include variations due to calibration uncertainties in addition to reflecting the wavelength-independent modeling technique). For example, the final single-scattering albedo values show a constant value of 0.049 between 1.86–2.0 μm , except at 1.91 μm where the value is 0.050. These values are equivalent within the grid size variations ($w: \pm 0.002$). The parameter variations in Figure 6 are mostly due to (1) the lower reflectance in the 2.7 μm absorption band, (2) a possible thermal contribution beyond 2.9 μm , and

(3) a drift of the opposition width with wavelength. Tests using smaller grid sizes show no significant ($\lesssim 0.2\%$) differences in the η values, thus the variation in the data set does not distinguish between parameter values at a finer resolution. This level of variation is due to differences within the data set from variations in Ryugu's surface reflectance.

The ratio between the observed reflectance to the model-predicted reflectance (Figure 7) was calculated in order to examine how well the model describes the data set. Values of unity correspond to equivalent values between the observation and model. Table 1 summarizes the percentage of the data sets that are described by the model to within 5% and 2% over the entire phase curve and within the narrow opposition range ($\alpha < 1^{\circ}$).

Another test of the modeling results is an examination and comparison of how well the model replicates the spectral properties of the spectral data set. Examples of spectral observations acquired near 15° phase (Figure 8) and within the opposition region (Figure 9) are contrasted with corresponding spectra derived from the Hapke model solutions. In the examples shown from the near 15° phase observations, there are good replications of the spectra by the model at 15.756° phase, yet poor replications at 15.766° phase. The 15.766° spectra provide an example of the variation within the data set and insight into how well the model captures that variation. Examination of the normalized spectra at both 15.766° and

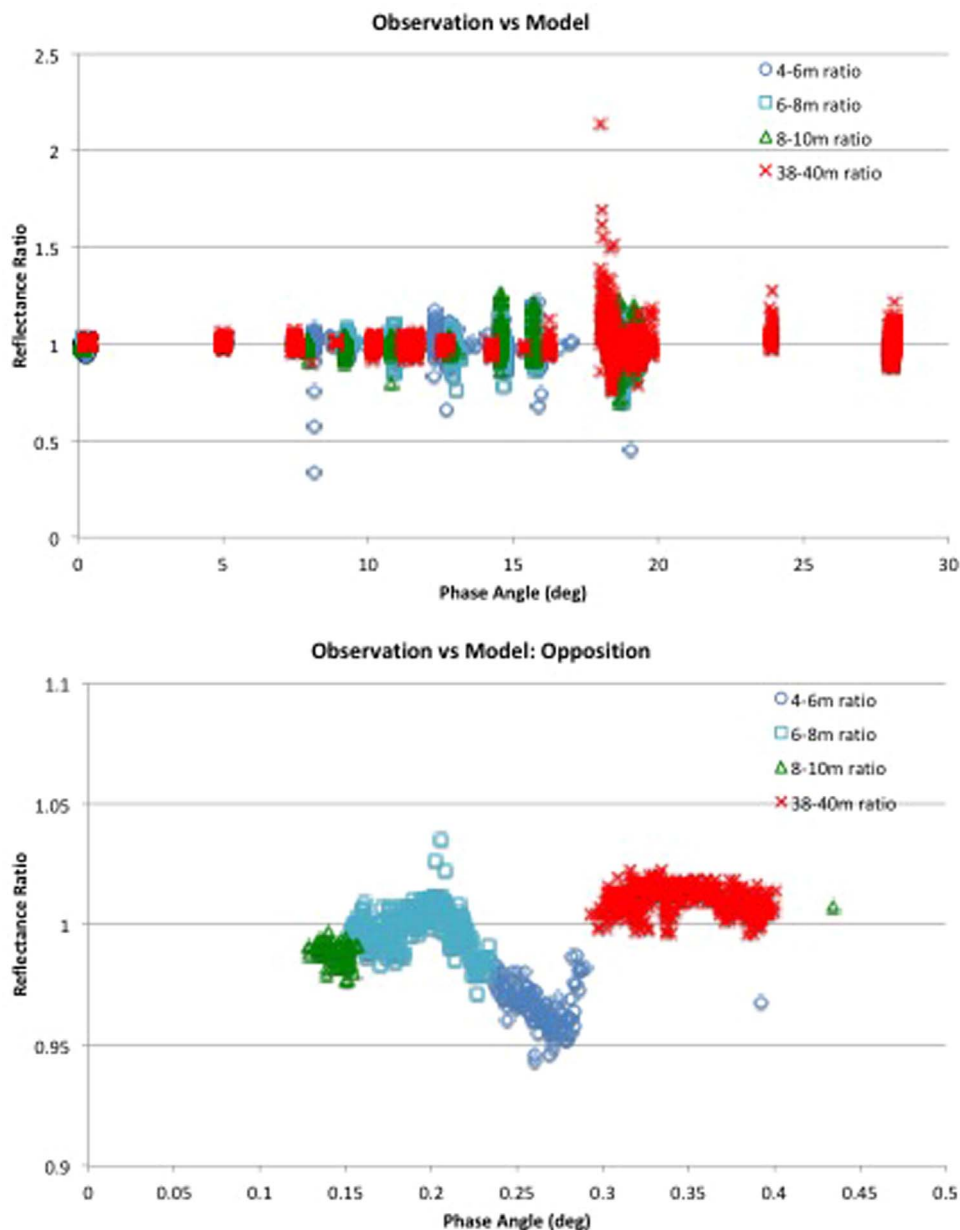


Figure 7. As a test of the goodness of fit, the ratio of the observed reflectance to the model-predicted reflectance is plotted as a function of phase angle for the $2.0 \mu\text{m}$ data set over all the footprint resolution groups. These results are typical of those seen across all wavelengths.

Table 1
Modeling Accuracy

Footprint Data Set	Entire Phase Angle Range		Opposition Region ($\alpha > 1^\circ$)	
	% within 5% of Unity	% within 2% of Unity	% within 5% of Unity	% within 2% of Unity
4–6 m	74.5	39.9	82.8	0
6–8 m	82.5	53.7	99.6	81.0
8–10 m	78.8	48.3	100	52.2
38–40 m	86.0	63.5	100	100

15.756° phase (Figure 8) show that both the observed spectra and their corresponding model spectra overlap, indicating that the photometric modeling captures the spectral slope and absorption properties inherent in the spectral data set. This is also observed at other phase angles. This suggests that the

variations we are seeing are due to either albedo or local roughness variations across the surface and not wavelength-to-wavelength (spectral) differences. A similar examination of the spectra acquired at near opposition geometries (Figure 9) shows that the model better predicts the spectral properties near opposition than at larger phase angles.

5. Comparisons with ONC-T

The NIRS3 and ONC observations of Ryugu examine both the spectral and photometric properties of its surface. Here we compare first the spectral and then the photometric properties of Ryugu as derived from each instrument. Because the wavelength regions of the two instruments do not overlap, we include ground-based observations in the comparison of the spectral properties to bridge the gap in wavelength coverage.

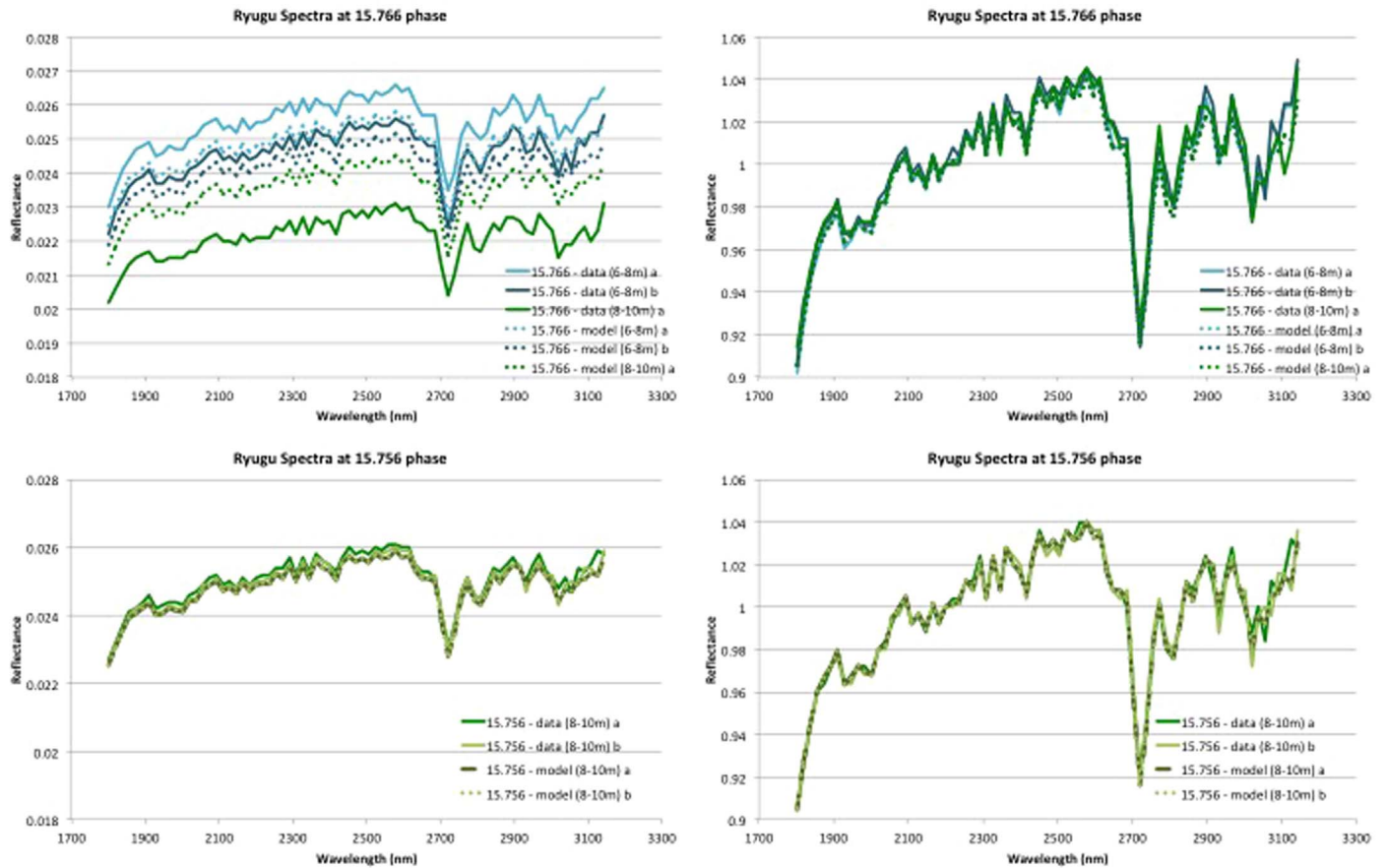


Figure 8. Comparisons of spectral observations from NIRS3 (solid lines) near 15° phase with the corresponding model-predicted spectra (dashed lines). Comparisons are made in absolute reflectance (left column) and normalized to unity at $2.2 \mu\text{m}$ (right column). Models are calculated using the same incidence, emission, and phase angle values as the observations.

5.1. Comparisons of Spectral Properties

The NIRS3 and ONC wavelength-dependent properties can be compared to understand their implications for regolith properties, such as granularity, grain size, and porosity/compaction. Examining general spectral properties, such as spectral slope and phase reddening, and comparing these properties with laboratory measurements of meteorites provide insight into these regolith properties.

Direct comparisons of the spectral properties of these two instruments are more difficult as the wavelength ranges do not overlap. In this case it is necessary to compare spectra from both instruments with ground-based observations to determine the visible to near-infrared spectral properties of Ryugu’s surface.

5.1.1. General Spectral Properties: Regolith Structural Implications

Comparisons of the NIRS3 opposition observations were made with the ONC-T color observations. Two sets of mosaics have been created from the ONC-T data set. One set of mosaics were constructed from images photometrically standardized to 30° , 0° , and 30° in incidence, emission, and phase, respectively (Tatsumi et al. 2020). This set consists of a global mosaic for each filter band of the camera system, and we hereafter refer to these global mosaics as the “standard mosaics”. The second set of mosaics was constructed from the ONC-T opposition observations, and they represent the normal albedo of the surface (Yokota et al. 2021). This set also consists of global mosaics, one for each band, and we hereafter refer to these global mosaics as the “normal albedo

mosaics”. The locations of the NIRS3 opposition observations are shown on the v -band standard mosaic in Figure 1.

Initial comparisons between the NIRS3 opposition spectra and the ONC-T observations were made by comparing the NIRS3 $2.0 \mu\text{m}$ band reflectance as a function of longitude with the ONC-T equivalent reflectance extracted from both the v -band standard mosaic and the v -band normal albedo mosaic as a function of longitude (Figure 10). The ONC-T equivalent spectra are derived from the global mosaics by projecting the NIRS3 footprint onto the mosaic and calculating the median value of the pixels contained within the footprint. The v -band equivalent reflectance values from both v -band mosaics show no reflectance differences as a function of footprint resolution. The NIRS3 reflectance values indicate that the smallest footprint resolution bin (4–6 m) is different than the remaining footprint resolution bins. However, the spread in reflectance values between the 4–6 m footprint resolution bin and the other NIRS3 footprint resolution bins is comparable to the spread seen in the v -band equivalent data (Figure 10). The range in reflectance values in the v -band equivalents is larger than the range seen in the NIRS3 $2.0 \mu\text{m}$ data.

Spectral properties that can be examined, and compared to laboratory studies of meteorites, include spectral slope and phase reddening. The spectral slope is defined as

$$\text{slope} = \frac{R_1 - R_2}{\lambda_1 - \lambda_2},$$

where R_1 and R_2 are the normalized reflectance values at wavelengths λ_1 and λ_2 , respectively. A spectrum is considered

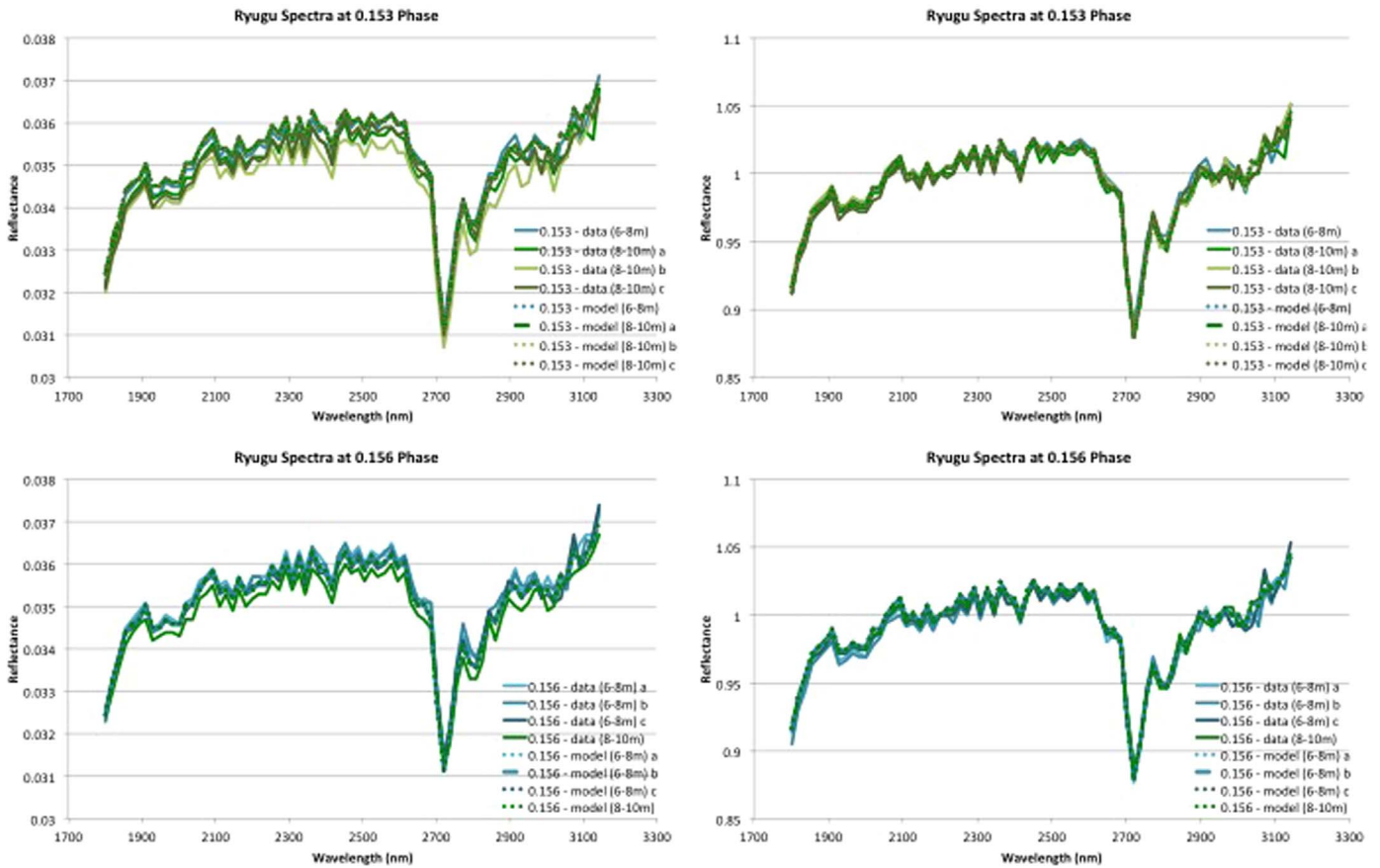


Figure 9. Comparisons of spectral observations from NIRS3 (solid lines) near opposition with the corresponding model-predicted spectra (dashed lines). Comparisons are made in absolute reflectance (left column) and normalized to unity at $2.2 \mu\text{m}$ (right column).

“red” or “red sloped” if it becomes brighter as wavelength increases, or the slope is positive. Conversely, a spectrum is considered “blue” or “blue sloped” if it becomes darker with increasing wavelength, or the slope is negative. Phase reddening (P_r , also called spectral reddening in the literature) is defined as

$$P_r = \frac{\text{slope}_{\alpha_1} - \text{slope}_{\alpha_2}}{\alpha_1 - \alpha_2},$$

where α_1 and α_2 are the phase angle values, and slope_{α_1} and slope_{α_2} are their corresponding slopes. Phase reddening occurs when P_r is larger than zero (slope increases with increasing phase angle), and phase bluing occurs when P_r is less than zero (slope decreases with increasing phase angle).

The spectral slope at the NIRS3 opposition footprint sites can be examined in both the visible and the near-infrared. Using the ONC-T data, the visible spectral slope was calculated using the *b*- and *p*-band reflectance values normalized to the *v* band. The slope was calculated for the locations of the NIRS3 opposition data from both the normal albedo mosaics of Yokota et al. (2021), and the standard mosaics of Tatsumi et al. (2020) (Figure 11). The standard mosaics represent the reflectance at 30° phase while the normal albedo mosaics represent the reflectance at 0° phase. The slope values derived from the normal albedo mosaics are blue while the corresponding values from the standard mosaic are red, thus indicating that the visible spectral properties become redder with increasing phase angle (Figure 11), commensurate with the studies of Sugita et al. (2019) and Tatsumi et al. (2020).

The spectral slope within the NIRS3 data was calculated based on the wavelength interval between $1.9 \mu\text{m}$ and $2.5 \mu\text{m}$ normalized to unity at $2.0 \mu\text{m}$, using the NIRS3 data from opposition ($\alpha < 0.5^\circ$) and again using data from 18.5° to 19.5° phase (Figure 12). The near opposition and near 19° phase slopes are both red, and in the near-infrared, Ryugu’s surface exhibits subtle phase reddening (becomes “redder”; the slope increases with increasing phase angle). The phase-reddening values are 4.5×10^{-6} , 4.2×10^{-6} , 4.4×10^{-6} , and 5.1×10^{-6} (units of $\mu\text{m}^{-1} \text{deg}^{-1}$) for the 4–6 m, 6–8 m, 8–10 m, and 38–40 m footprint bins, respectively. These values are calculated from the median spectral slope for each footprint bin for both the near opposition and near 19° phase spectra. This is in comparison to the visible phase-reddening values of 3.9×10^{-3} , 4.4×10^{-3} , 3.4×10^{-3} , and 2.4×10^{-3} (units of $\mu\text{m}^{-1} \text{deg}^{-1}$) for the 4–6 m, 6–8 m, 8–10 m, and 38–40 m footprint bins, respectively, calculated from the normal albedo and standard mosaics (Figure 11). The visible phase-reddening values are higher than those calculated by Tatsumi et al. (2020) of $(8 \pm 5) \times 10^{-4} \mu\text{m}^{-1} \text{deg}^{-1}$, which is based on a disk-integrated data set. Thus, phase reddening is observed in both visible and near-infrared spectra of Ryugu, although it is subtle and much shallower in the near-infrared wavelength range.

There have been many laboratory examinations of meteorite samples that have attempted to correlate spectral slope and phase-reddening properties with asteroid regolith characteristics (e.g., Beck et al. 2012; Binzel et al. 2015; Cloutis et al. 2018). For example, Beck et al. (2012) examined a series of meteorite samples over five different bandpass filters in the

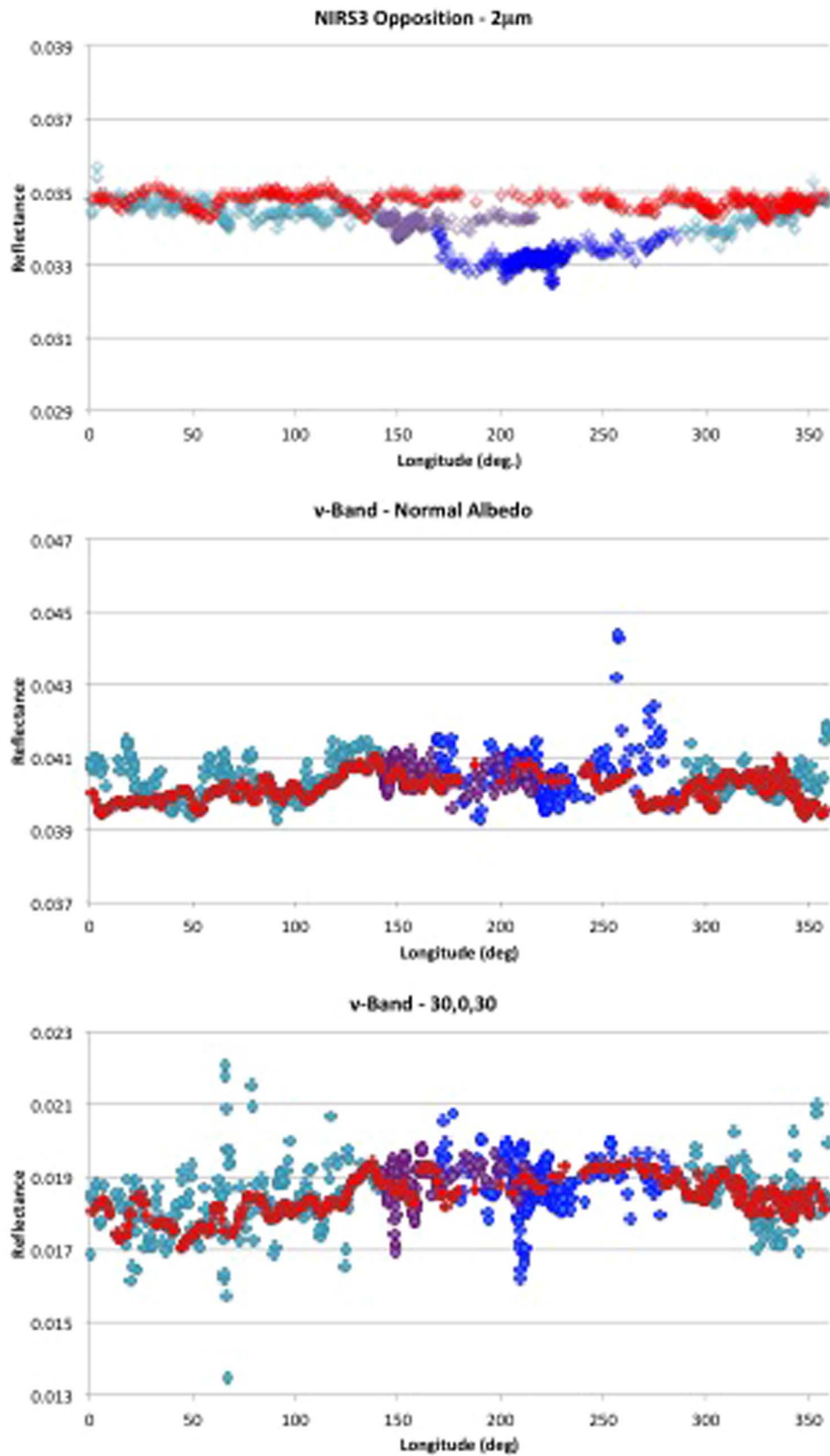


Figure 10. Reflectance variation within the NIRS3 opposition data (top) acquired at phase angles $<5^\circ$ is compared with the NIRS3-equivalent footprint resolution data extracted from the ONC-T v -band standardized mosaic (center; Tatsumi et al. 2020) and the ONC-T v -band normal albedo mosaic (bottom; Yokota et al. 2021). Size group colors as in Figure 1. Phase angles below 1° range from $0^\circ293$ – $0^\circ401$ for the 4–6 m resolution bin, $0^\circ150$ – $0^\circ233$ for the 6–8 m resolution bin, $0^\circ128$ – $0^\circ434$ for the 8–10 m resolution bin, and $0^\circ293$ – $0^\circ401$ for the 38–40 m resolution bin.

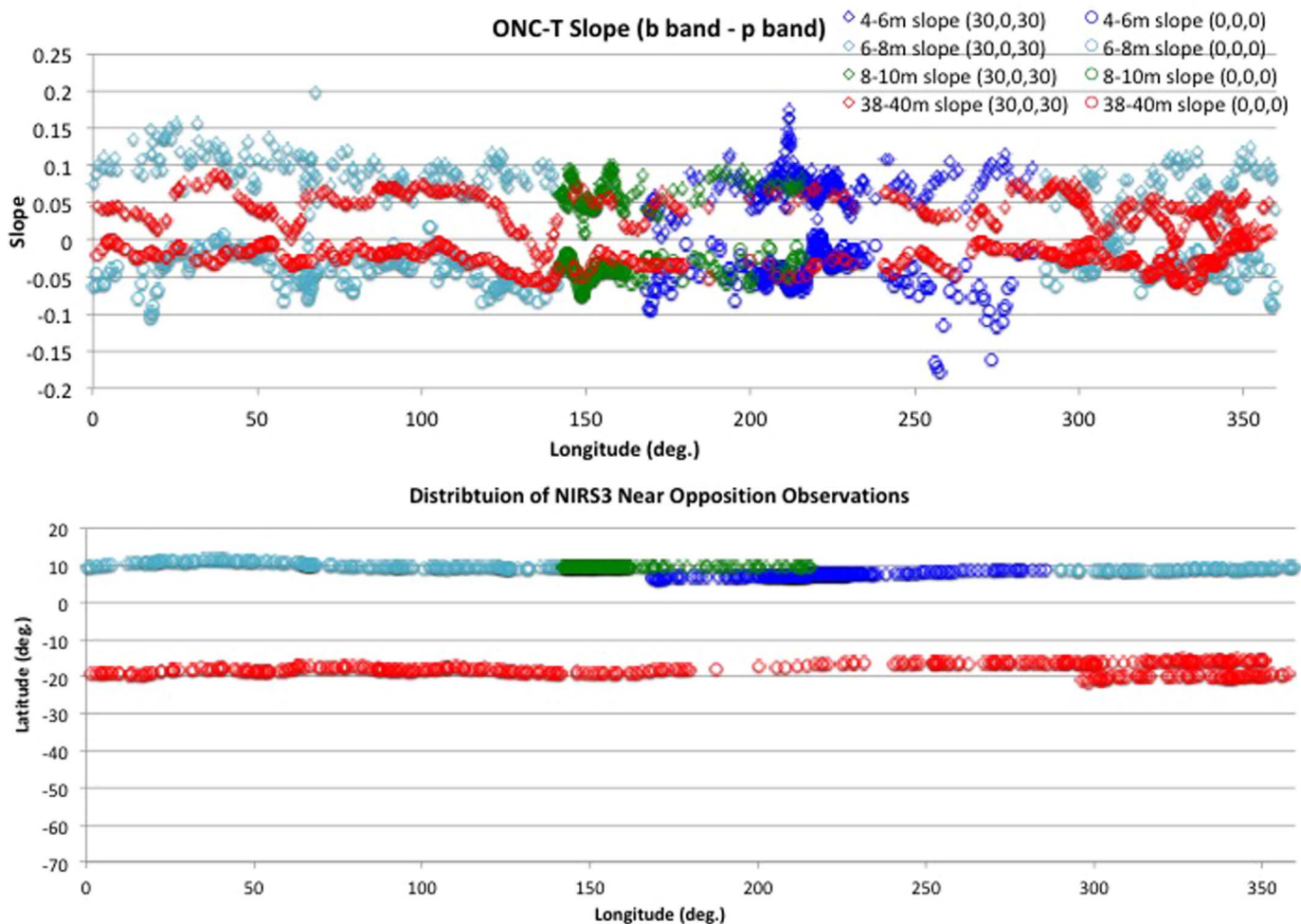


Figure 11. (Top) The spectral slope calculated from the ONC-T standardized mosaics (open diamonds) of Tatsumi et al. (2020) and the normal albedo mosaics (open circles) of Yokota et al. (2021) of the ONC-T equivalent reflectance to the NIRS3 opposition data in units of μm^{-1} . The slopes were calculated using the *b*- and *p*-band reflectance values. The colors correspond to the footprint sizes (blue 4–6 m, teal 6–8 m, green 8–10 m, and red 38–40 m). Subtle regional variations are noted in the spectral slope values. (Bottom) The longitudinal and latitudinal coverage of the opposition observations.

visible ($0.45\text{--}0.9\ \mu\text{m}$) that included three carbonaceous chondrites (Orgeuil (CI), Tagish Lake (CC), and Allende (CV)) along with a howardite, eucrite, diogenite, and a lunar meteorite. All samples they examined displayed phase reddening. This trend with phase angle was seen in samples with both blue and red spectral slopes. This trend, also seen in studies of basalt and Allende meteorite (Gradie et al. 1980; Gradie & Veveřka 1986), led Beck et al. (2012) to assert that phase reddening is ubiquitous to all meteorite types. More detailed laboratory work examined the correlations of spectral slope and spectral reddening with sample properties, such as granularity (rock versus powder), grain size, packing (porosity), and surface texture (roughness). The goal is to extrapolate these correlations to characterize the physical properties of asteroid surface regoliths. The findings are summarized and compared to our findings for Ryugu.

Granularity. Cloutis et al. (2018) examined and compared the spectral slope of samples of the Murchison meteorite, a CM2 carbonaceous chondrite, finding that slab samples were darker and blue sloped in comparison with powdered samples. Examination of the Mukundpura CM2 chondrite by Potin et al. (2019) also correlated spectral effects as a function of rock versus powder. Potin et al. (2019) demonstrated that for

samples of this CM2 meteorite, even though both powder and rock have red slopes, powder displays a redder spectral slope than the bare rock, and powder also displays greater phase reddening than rock. In their experiments they discovered that spectral slope is affected by incidence angle, where the powder sample was relatively insensitive to incidence but the rock sample displayed a strong sensitivity, especially at grazing (high) values of incidence. The effect they noted is that at the same phase angle, the spectral slope becomes redder with increasing incidence angle in their rock sample. This could be used as a test for the presence of powdered regolith on an otherwise rocky surface.

Examination of the NIRS3 38–40 m footprint data as a function of incidence angle at both opposition and near 19° phase (Figure 13) shows no definitive correlation in the spectral slope with incidence angle. This argues for a “powder” component to Ryugu’s regolith, based on the laboratory measurements described by Potin et al. (2019).

Grain size. Binzel et al. (2015) examined Murchison samples of various grain sizes and demonstrated that while coarse-grained samples ($500\text{--}1000\ \mu\text{m}$ grains) are spectrally blue, the introduction of even 5% of fine-grained fraction ($<45\ \mu\text{m}$ grain size) changes the slope from blue to red. Increasing average grain size, for

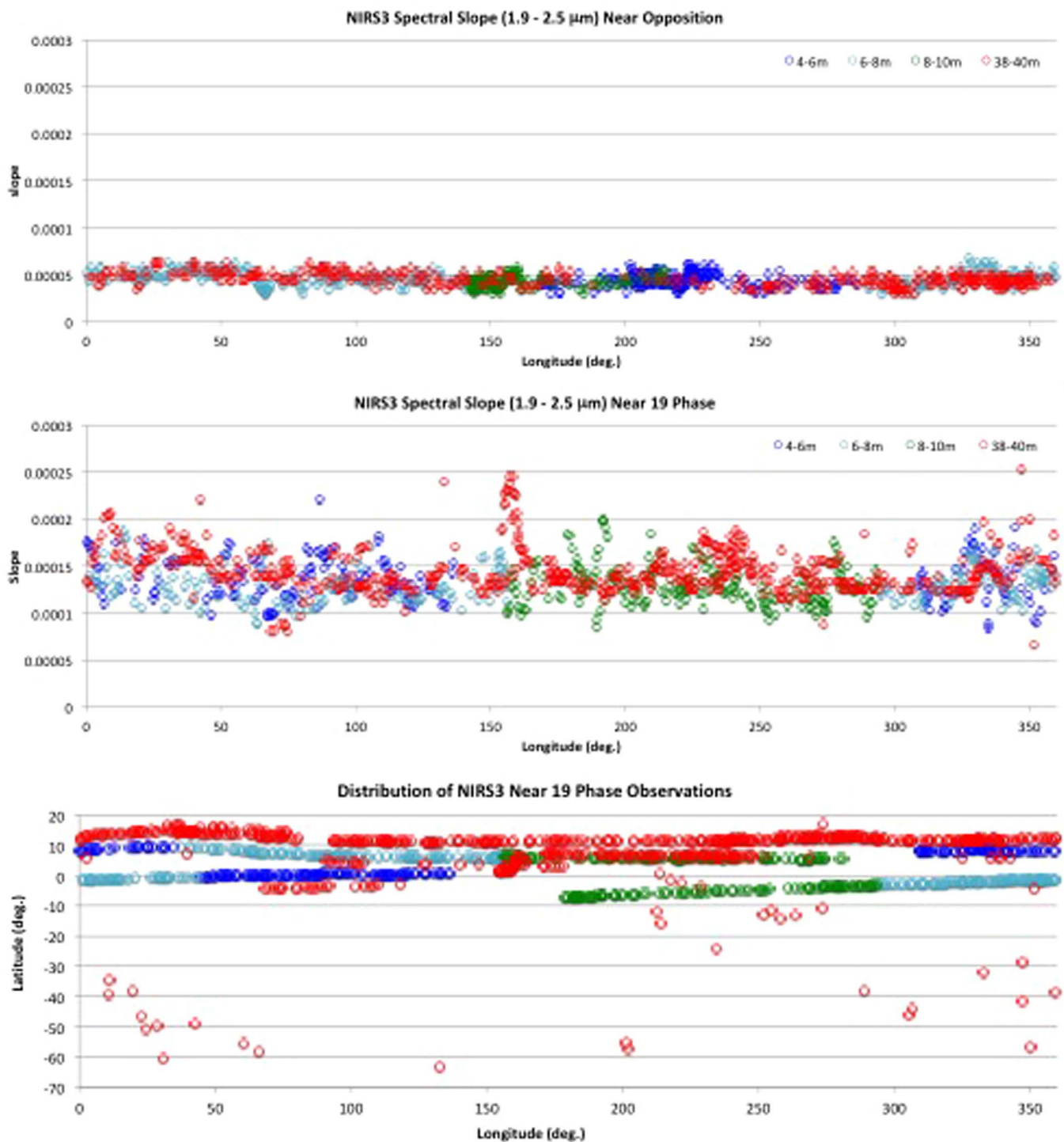


Figure 12. The spectral slope calculated from NIRS3 opposition observations (top) and the near 19 phase angle observations (center). The slopes were calculated using based on the 1.9 and 2.5 μm reflectance values. The colors correspond to the footprint sizes (blue 4–6 m, teal 6–8 m, green 8–10 m, and red 38–40 m). The longitudinal and latitudinal coverage of the near 19° phase observations (bottom) can be compared with the similar coverage for the opposition observations shown in Figure 13.

carbonaceous chondrites, results in darker more blue-sloped spectra (Johnson & Fanale 1973; Gillis-Davis et al. 2013; Cloutis et al. 2011, 2013; Binzel et al. 2015; Cloutis et al. 2018), whereas the inclusion or presence of a fine-grained fraction introduces spectral reddening (Schröder et al. 2014; Binzel et al. 2015; Cloutis et al. 2018). The spectral slopes here refer to the brightness variation at wavelengths above 0.7 μm . Cloutis et al. (2018), in their study of Murchison powders, demonstrated that the greatest

influence on spectral slope was the minimum grain size of the sample, not the average or maximum grain size. They showed that as the grain size decreases, spectra become brighter and redder sloped, commensurate with the findings of Binzel et al. (2015).

Our analyses of the visible spectral slope properties show that at opposition, Ryugu’s surface is blue sloped, whereas at larger phase angles (commensurate with those of the laboratory studies) the surface is red sloped. In the infrared the spectral

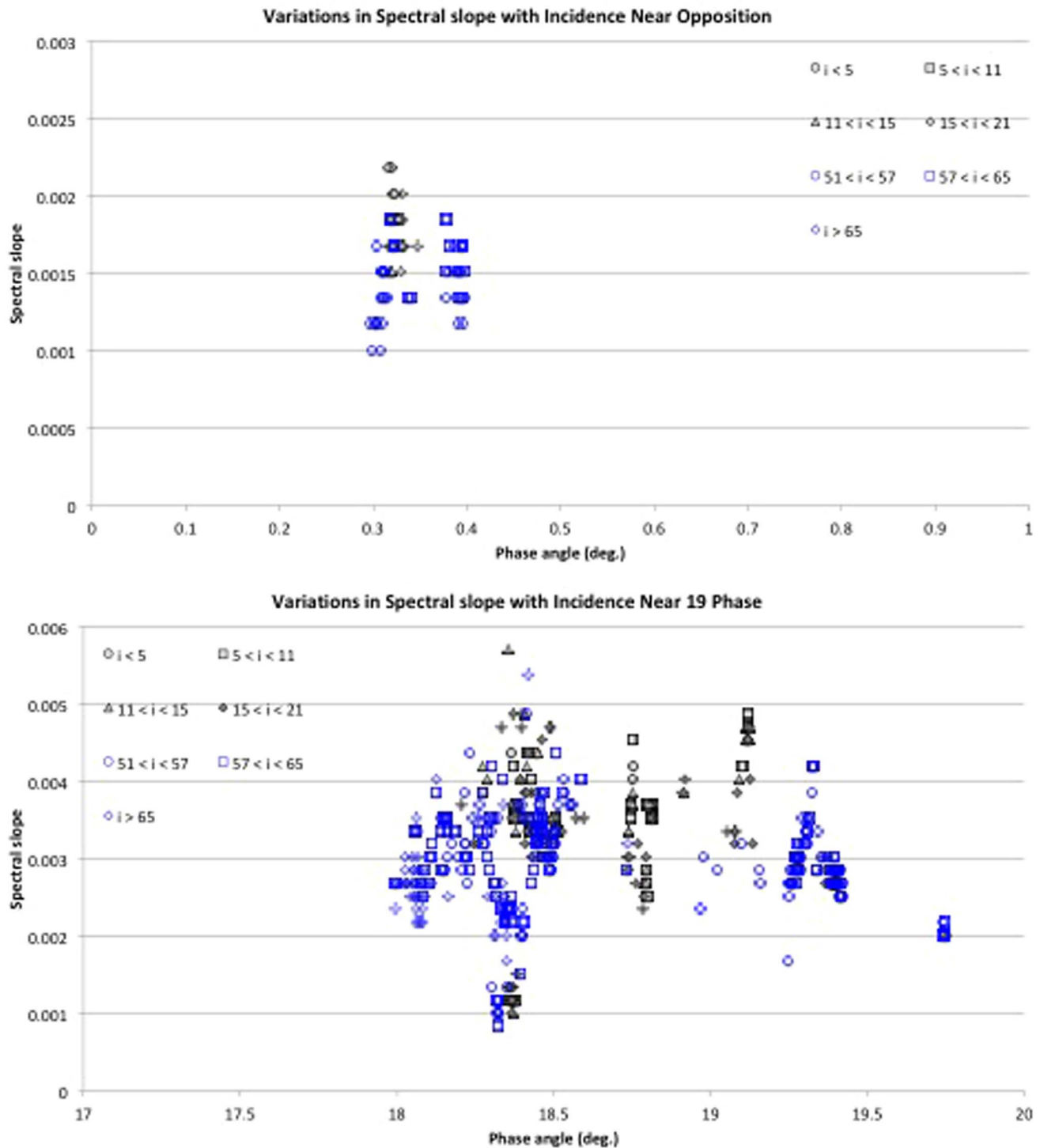


Figure 13. Comparisons of spectral slope at (top) opposition phase angles and (bottom) near 19° phase as a function of near nadir (low incidence; black symbols) and grazing (high incidence; blue symbols). No distinctive trend with incidence angle suggests the presence of a granular component at the surface of Ryugu.

slope is red at both opposition and larger phase angles. Cloutis et al. (2018) demonstrated that slabs of a CM chondrite are blue, which would be expected of a surface with no granular regolith. Binzel et al. (2015) demonstrated that coarse-grained regolith also displays a blue spectral slope and that a fine-grained component was needed to produce a red spectral slope. Both the ONC-T and NIRS3 spectral observations show a red spectral slope for Ryugu’s surface, providing another indication of the presence of a “powder” component within Ryugu’s

regolith and that this component contains a fine-grained fraction.

Packing/porosity. The study by Cloutis et al. (2018) found that the spectral effects of sample packing or porosity was connected to the incidence, emission, and phase angle conditions under which the spectra were acquired. At the standard laboratory conditions ($i = 30^\circ$, $e = 0^\circ$, $\alpha = 30^\circ$) they found that there were no effects on spectral slope with packing; however, they found that spectral slope increased (became redder) with

increasing porosity for spectra acquired at $i = e = 45^\circ$. This is commensurate with the findings of Lantz et al. (2017), who demonstrated that unpacked powders of carbonaceous meteorite samples were darker and redder than the same samples compacted into pellets. There is currently no metric to correlate spectral slope with a specific packing or porosity value; however, this can provide a metric for potentially mapping the relative packing differences across a surface. More work is needed to understand how to distinguish between the spectral slope changes due to grain size from packing.

In the case of Ryugu, the observation that compaction creates bluer, brighter spectra suggests that the red spectral slope implies some amount of porosity in the regolith.

Surface texture/roughness. Binzel et al. (2015) examined the spectral properties (between 400 and 2500 nm) of saw-cut faces of Murchison that displayed variable amounts of surface roughness. They found the spectral slope ranged from overall blue to strongly red, suggesting that surface roughness affects spectral slope in a regolith-free environment; however, they do not state if rougher surfaces are bluer or redder. Binzel et al. (2015) also examined powders of Murchison. In one case they examined a powdered sample of Murchison with a grain size of $<150 \mu\text{m}$ under various particle densities and surface textures. Their conclusion was that surface texture and particle density can change the overall spectral slopes of carbonaceous chondrites, though they do not correlate specific textures and densities with bluer or redder slopes. Cloutis et al. (2018) found that surface texture had a larger effect on the photometric properties of the samples with no clear correlation with spectral slope or reddening.

Space weathering. Laboratory experiments of “traditional” space weathering processes (solar wind radiation and micro-meteoritic bombardment) on carbonaceous asteroids show both spectral reddening and bluing (e.g., Moroz et al. 2004; Nesvornyy et al. 2005; Lazzarin et al. 2006; Hiroi et al. 2013; Lantz et al. 2013; Vernazza et al. 2013; Brunetto et al. 2014; Lantz et al. 2015; Matsuoka et al. 2015; Gillis-Davis et al. 2017; Lantz et al. 2017; Thompson et al. 2019; Matsuoka et al. 2020; Nakamura et al. 2020; Thompson et al. 2020). A solar heating (another space weathering process) study by Hiroi et al. (1993) shows that carbonaceous chondrite samples display bluer slopes when heated. The properties of the spectral slope are ambiguous for linking traditional space weathering processes to surface alteration, but may be indicative of heating events. More laboratory work is needed to make a definitive claim.

5.1.2. Ryugu’s Visible to Near-infrared Spectral Properties

The NIRS3 spectral data set can be compared with both the ONC color and ground-based observations. The normalized near-infrared observations of Moskovitz et al. (2013) and Le Corre et al. (2017) are compared to a subset of the 38–40 m footprint resolution NIRS3 opposition spectra (Figure 14). All spectra are normalized to unity at $2.0 \mu\text{m}$ and show a similar spectral shape in the wavelength range of overlap between the three data sets. Even though the spectra overlap within the noise of the ground-based observations, the NIRS3 spectra suggest a shallower slope at longer wavelengths. The ground-based observations show differences in the spectral slope at shorter wavelengths approaching the visible and do not overlap below $\sim 1.4 \mu\text{m}$.

Examination of the Moskovitz et al. (2013) normalized visible spectra, in comparison with their near-infrared spectrum

(Figure 15—center), suggests that Ryugu’s spectrum is flat in the visible and increases in slope toward the near-infrared. These data have been normalized to unity at $0.86 \mu\text{m}$. Comparison of the Moskovitz et al. (2013) visible spectra renormalized to unity at $0.55 \mu\text{m}$ with the ONC color observations also normalized to unity at $0.55 \mu\text{m}$ demonstrates that the shape of the two spectral data sets are similar (Figure 15—bottom). However, comparisons of the ONC color with the NIRS3 spectra in absolute reflectance (Figure 15—top) show a different relationship between the visible and near-infrared than seen in the ground-based observations, outside of what could be ascribed to differences due to phase angle variations. The visible reflectance is brighter than the near-infrared, which is opposite to the relationship seen in the Moskovitz et al. (2013) spectral observations (Figure 15—center). The source of this spectral difference between the two instruments is currently unknown.

5.2. Comparisons of Photometric Properties

The ONC-T approach observations were modeled by Tatsumi et al. (2020) using the Hapke set of equations. Their results are compared to those from this study of the NIRS3 opposition data set. It is important to note that the ONC-T study included both disk-integrated and disk-resolved observations. The ONC values are derived from disk-integrated measurements constrained by disk-resolved measurements, but the NIRS3 values are derived solely from disk-resolved values. The ONC-T data set also covered a larger range of phase angle, which include disk-integrated opposition measurements. The surface roughness parameter from the ONC-T study was $28^\circ \pm 6^\circ$ (Tatsumi et al. 2020) whereas the NIRS3-based value is $29^\circ \pm 3^\circ$, both identical within the error bars. The NIRS3 study found a uniform value of 0.318 for the single-particle scattering parameter, b , whereas the ONC-T values ranged from 0.374 to 0.388 with a median value of 0.386 across all ONC-T bands (Tatsumi et al. 2020). The values correspond to a backward-scattering phase function from both instrument data sets, with a more strongly backward-scattering, particle-scattering function in the visible.

The spectral characteristics of the single-scattering albedo for both instrument data sets are similar in shape to the spectral properties (Figure 16). While the near-infrared spectra from the NIRS3 are darker than their counterpart visible spectra (Figure 15) from the ONC-T, the opposite is seen for the single-scattering albedo derived from each instrument’s data set. The relative values in single-scattering albedo between the visible and near-infrared are similar to what is seen in the ground-based spectral observations. The single-particle scattering function is less strongly backward scattering in the NIRS3 modeling results, which results in a darker reflectance, thus the absolute reflectance differences between the visible (ONC) and near-infrared (NIRS3) are accounted for by the model in the single-particle scattering function.

The opposition parameter values from the ONC-T study were assumed constant with wavelength over the instrument’s band range ($0.40\text{--}0.95 \mu\text{m}$), because the wavelength-to-wavelength variation was minor (Tatsumi et al. 2020). The opposition parameter values from the ONC-T study are based on visible disk-integrated opposition observations, in contrast to the NIRS3 opposition data set that consists of near-infrared disk-resolved measurements. Thus, the ONC parameters describe the globally averaged surface, whereas the NIRS3 parameters describe the near-equatorial region they observe. The disk-resolved opposition

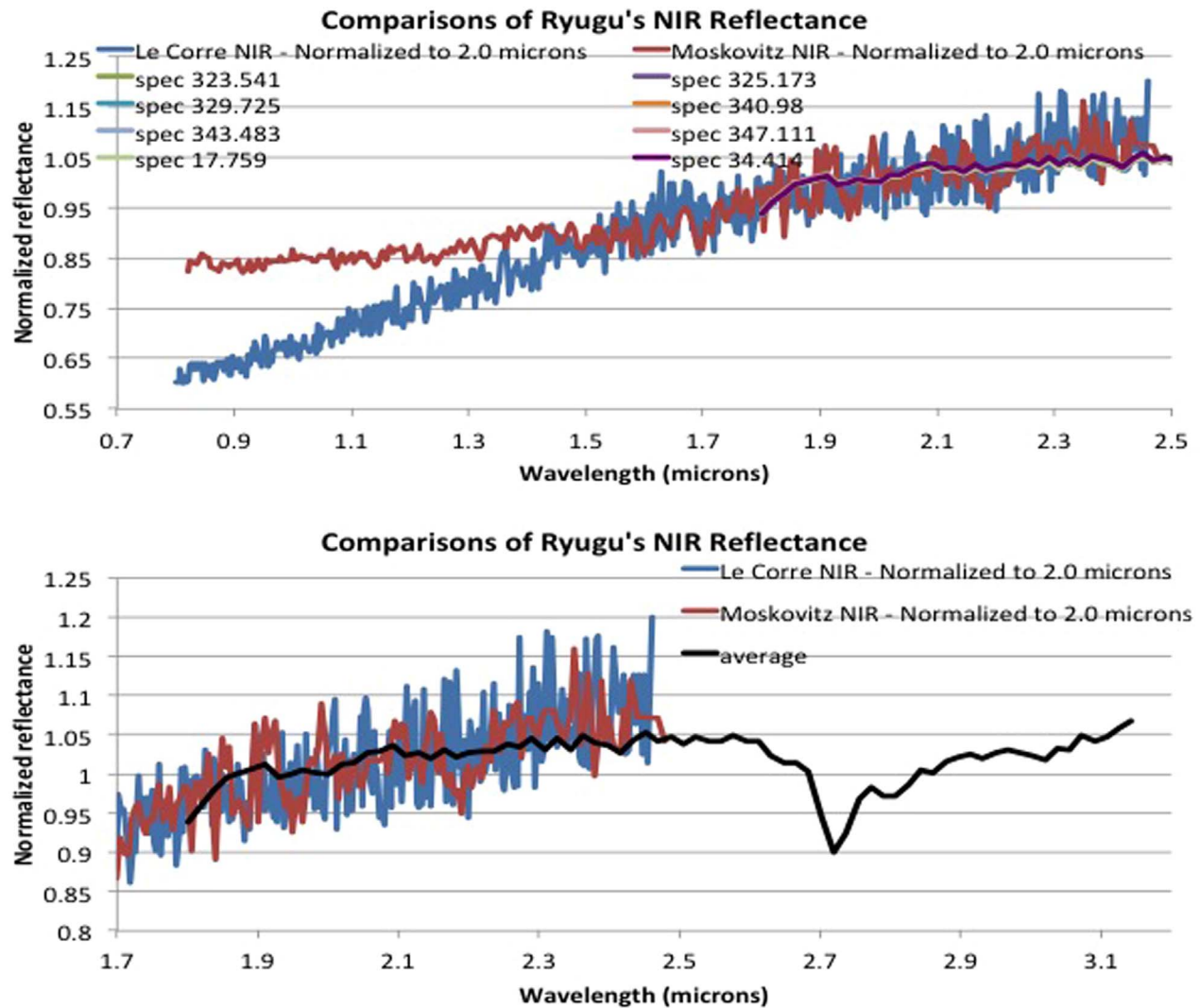


Figure 14. Example opposition spectra from the 38–40 m footprint resolution bin across several longitudes (identified in the upper graph’s legend, which overlap sufficiently that only the last spectrum, in purple, is clearly visible) from the NIRS3 data set are compared to the ground-based observations of Le Corre et al. (2017) in blue and Moskowitz et al. (2013) in red. All spectra are normalized to unity at 2.0 μm . The average of the example NIRS3 spectra is compared over the near-infrared wavelengths (bottom graph).

observations from the NIRS3 data show that in the near-infrared, there are variations with wavelength (Figure 16). The variations in the opposition parameters derived from the NIRS3 data appear to be centered about the 2.72 μm feature and may be due to differences caused by the material creating this absorption. This is discussed in more depth in Section 6.

6. Regolith Characteristics

In order to interpret the opposition parameters, it is helpful to understand their definitions and the assumptions inherent in their definitions. The opposition amplitude is defined as the amount of light from the first reflection ratioed to the total reflection at $\alpha = 0$. Based on the definition of B_o , changes in the opposition amplitude correspond to changes in the amount of light initially scattered versus the amount of light totally scattered into the opposition direction. A value of $B_o = 1$ can then be interpreted as all the light is scattered from the first reflection into the opposition direction. Decreases in B_o correspond to an increase in the mechanisms that decrease the amount of light initially scattered, or an increase in

absorption or transmission of light as opposed to reflection. The general correspondence of the decrease in B_o with the 2.72 μm absorption feature is commensurate with these mechanisms (less light is reflected, more light is absorbed). The additional wavelength structure in B_o implies that the optical properties of the material within Ryugu’s regolith are more complex than what is seen in the spectral reflectance alone. Thus, the variations in the opposition surge amplitude with wavelength are attributable to the physical properties of the regolith and not simply the albedo of the regolith.

The opposition width parameter’s value, based on the Hapke model derivation, is related to the porosity and grain size distribution within the optically active portion of the regolith. Hapke (2012) defines the half-width at half-maximum of the shadow-hiding opposition surge, h , as

$$h = \frac{KEa_E}{2},$$

where K is the porosity coefficient, E is the volume-averaged extinction coefficient, and a_E is the mean extinction radius (the

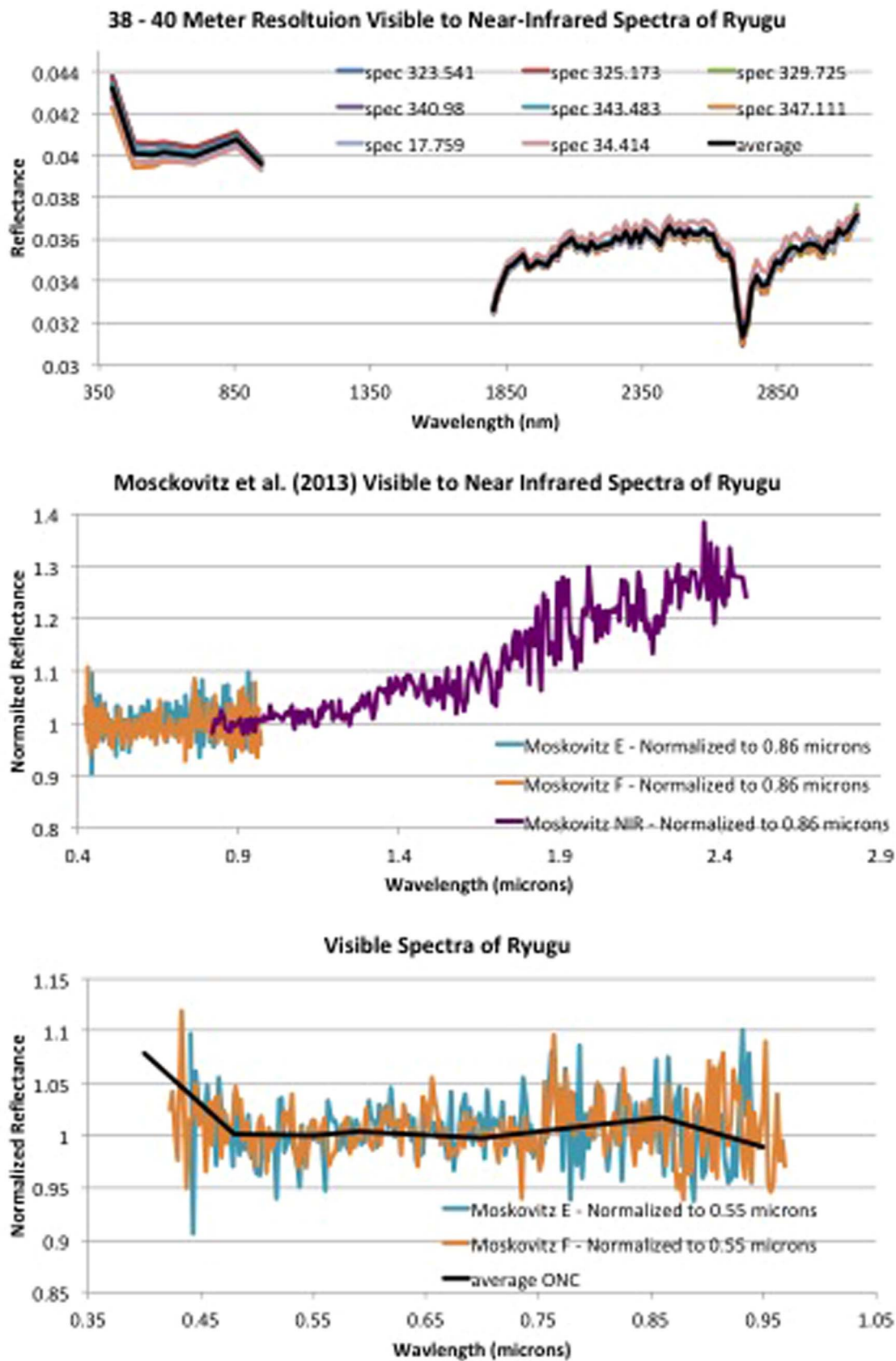


Figure 15. The observations of Moskovitz et al. (2013), shown in the center graph, display a smooth, increasing slope from the visible to the near-infrared. This comparison is made by normalizing both the visible and near-infrared observations to unity at 0.86 μm . Renormalizing the visible spectra to unity at 0.55 μm shows that the ONC color spectra display the same shape as the ground-based data (bottom graph). However, comparisons of the ONC color and NIRS3 spectra (top graph) in absolute reflectance show that the visible spectrum is brighter than the near-infrared. The ONC spectra are the NIRS3-equivalent spectra derived from the normal albedo mosaics. The average spectrum shown in the top graph is the same spectrum shown in the bottom graph.

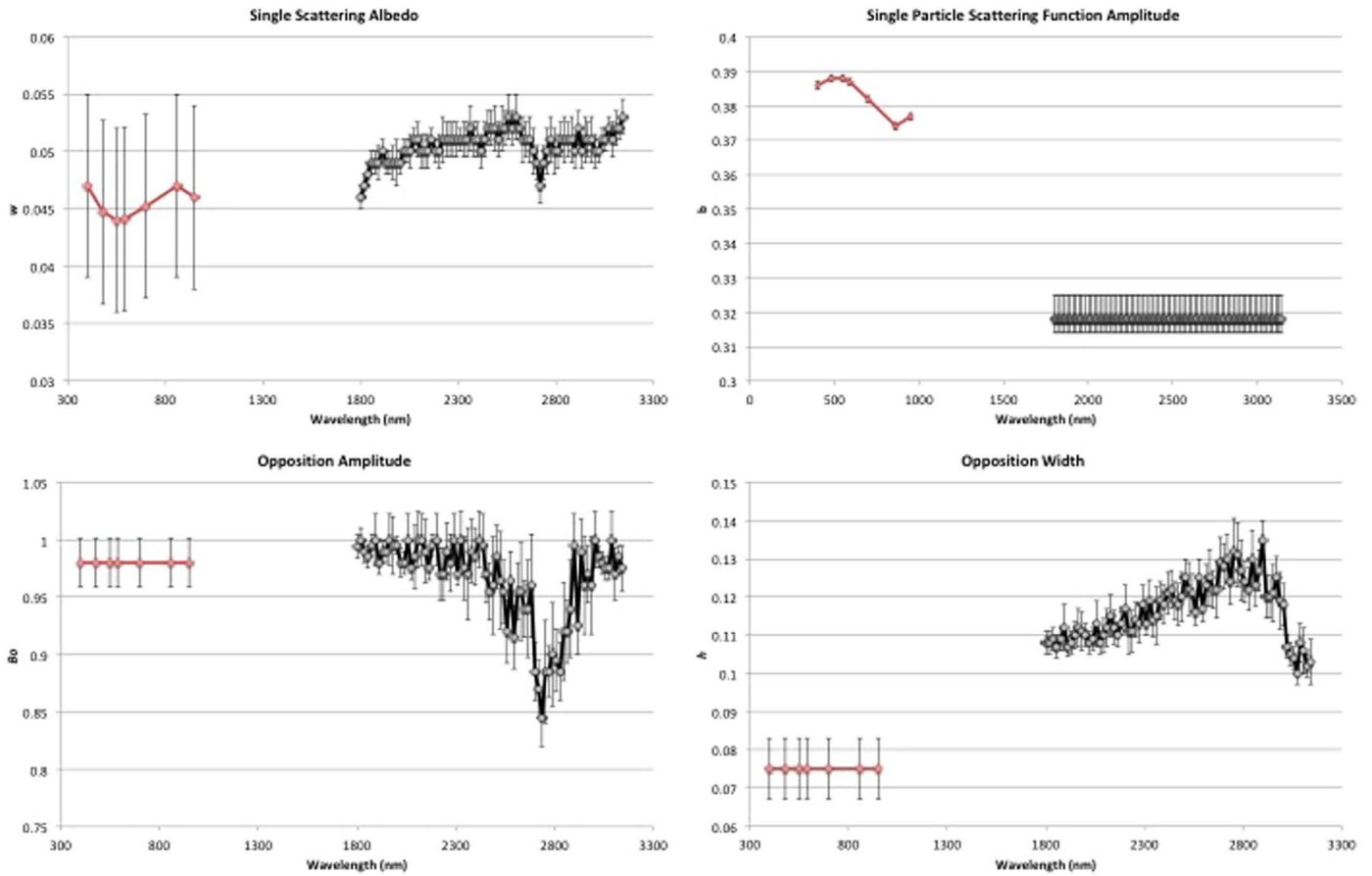


Figure 16. Comparisons of the wavelength variability of the Hapke model parameter values from the ONC-T study (Tatsumi et al. 2020) with those acquired in this study for the NIRS3 opposition data. The black lines are the NIRS3 values, and the red lines are the ONC-T values. Note that the opposition parameters from the ONC-T study were set to be constant over wavelength, whereas the single-particle scattering function amplitude was set to be constant in the NIRS3 data analysis. The error bars for the ONC-T b values (top right) are nearly equivalent to the symbol size.

radius of an equivalent sphere having a cross-sectional area equal to σ_E , the volume-average extinction cross section). The porosity of the optically active portion of the regolith is wavelength invariant. However, the extinction coefficient and cross section are dependent on the composition and physical structure of the grains within the regolith and can vary with wavelength.

Hapke (1981, 1984, 1986, 2002, 2008, 2012) argues that if the particles are larger than the wavelength of observation and equant, and the particle size distribution is narrow, then the volume-average extinction efficiency can be assumed to be approximately unity, a_E is approximately equal to the particle radius (a), and σ_E is $\cong \pi a^2$. In this case, the opposition width, h , is related to porosity and grain size by

$$h = -\left(\frac{3}{8}\right)Y \ln(\rho),$$

where ρ is the porosity and Y is the grain size distribution function, which is related to the power-law index β of the differential size distribution of grains (ratio of the radius of the largest to smallest grain size). These assumptions imply no wavelength-dependent variations in the extinction properties of the regolith material, thus the opposition parameters would be constant as a function of wavelength. This is clearly not the case for Ryugu in the near-infrared. The wavelength dependence seen in the opposition parameter values implies one or

more of the above assumptions do not apply to Ryugu's regolith. Therefore, the variations in the opposition surge width with wavelength are also attributable to the physical properties of the regolith and not simply the regolith's albedo.

The values of both B_o and h support wavelength-dependent physical characteristics of the regolith. These characteristics include the extinction coefficient of the regolith grain material, the mean extinction radius, and that at least one of these characteristics does not apply to Ryugu's regolith: grains are larger than the observing wavelength, grains are equant, and the size distribution of the grains is narrow. Based on the spectral slope and phase-reddening properties, along with the imaging of the surface, the grain size distribution is neither equant or narrow, in line with the properties we see in the opposition parameters.

Comparisons of the opposition parameter values derived for Ryugu with other solar system objects (Figure 17 and Table 2) allow us to make some inferences based on comparative planetology. However, the objects in Figure 17 (also listed in Table 2) were modeled using different strategies depending on the quantity and quality of the data being modeled. All objects listed, with the exception of Mathilde, are brighter than Ryugu, thus many studies include a mechanism for including a CBOE. For many of the published studies, the CBOE was accounted for by allowing values of B_o to exceed unity. Applications of the Hapke model, which explicitly accounts for CBOE, were applied to asteroid 21 Lutetia by Hasselmann et al. (2016) and

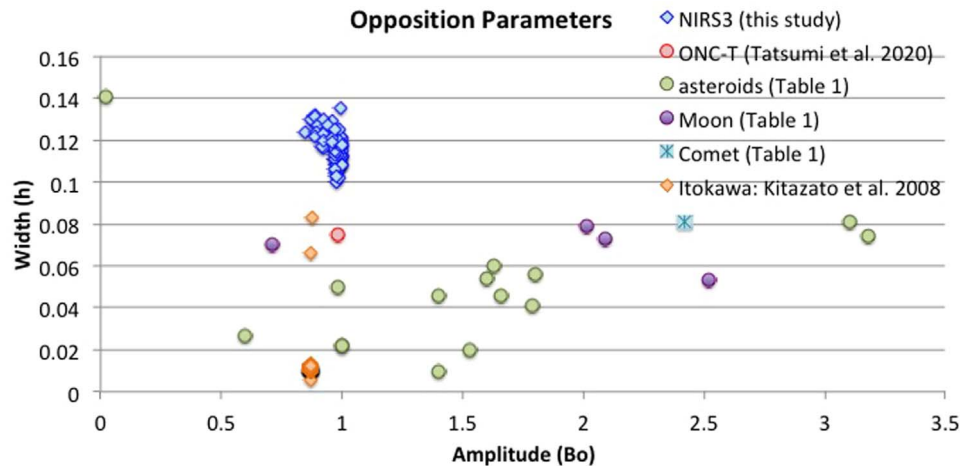


Figure 17. Comparisons of the values of the opposition amplitude (B_o) with the opposition width (h) for several solar system objects. The Ryugu values from this study (blue diamonds) are plotted with those from the ONC-T (red circle), those from other asteroids (green circles), the Moon (purple circles), and comet 67P/CG (blue asterisk). The values from the near-infrared study of Itokawa by Kitazato et al. (2008, orange diamonds) are also shown. Table 2 shows the values for the specific objects that are being compared with the NIRS3-derived parameter values. NOTE: the comparison is being made between the NIRS3 near-infrared values with visible wavelength values of other objects, with the exception of the modeling results of Itokawa by Kitazato et al. (2008).

Table 2
Comparisons of Opposition Parameter Values^a

Asteroid	Taxonomy (system)	B_o	h	Reference
162173 Ryugu	Cb/Cg (Binzel)	0.98 ± 0.02	0.075 ± 0.008	Tatsumi et al. (2020)
25143 Itokawa	S(IV) (Tholen)	0.98 ± 0.06	0.05 ± 0.02	Tatsumi et al. (2018)
25143 Itokawa	S(IV) (Tholen)	0.02 ± 0.1	0.141 ± 0.1	Lederer et al. (2008)
25143 Itokawa	S(IV) (Tholen)	$0.867\text{--}0.872 \pm 0.013^b$	$0.006\text{--}0.083 \pm 0.031^b$	Kitazato et al. (2008)
433 Eros	S/Sw (Tholen/Bus Demeo)	1.00 ± 0.14	0.022 ± 0.005	Clark et al. (2002)
433 Eros	S/Sw (Tholen/Bus Demeo)	1 ± 0.02	0.022 ± 0.005	Domingue et al. (2002)
433 Eros	S/Sw (Tholen/Bus Demeo)	1.4 ± 0.1	0.010 ± 0.004	Li et al. (2004)
253 Mathilde	Cb (Bus)	3.18	0.074	Clark et al. (1999)
951 Gaspra	S (Tholen)	1.63 ± 0.07	0.06 ± 0.01	Helfenstein et al. (1994)
243 Ida	S/Sw (Tholen/Bus Demeo)	1.53 ± 0.01	0.02 ± 0.005	Helfenstein et al. (1996)
2867 Steins	E	0.60 ± 0.05	0.027 ± 0.002	Spjuth et al. (2012)
21 Lutetia	M/Xc (Tholen/Bus Demeo)	(1.79)	(0.041)	Masoumzadeh et al. (2015); Hasselmann et al. (2016)
4 Vesta	V (Tholen/Bus Demeo)	1.66	0.076	Li et al. (2013)
1 Ceres	G/C (Tholen/Bus Demeo)	3.1	0.081	Schröder et al. (2018)
		1.8	0.056	
		1.6	0.054	
67P/CG	Comet	2.42 ± 0.3	0.081 ± 0.005	Hasselmann et al. (2017)
Moon		0.71	0.07	Helfenstein & Veverka (1987)
Moon (average)		2.01	0.079	Sato et al. (2014)
Moon (highlands)		2.09	0.073	Sato et al. (2014)
Moon (mare)		2.52	0.053	Sato et al. (2014)

Notes.

^a All asteroid parameter values are for the v -band equivalent wavelength, with the exception of Steins (630 nm), Lutetia (631.6 nm), and Itokawa (763–2247 nm; Kitazato et al. 2008).

^b Minimum and maximum values are listed, errors are averaged over the entire wavelength range. Numbers in brackets were held constant during some portion of the modeling analysis.

comet 67P/CG by Feller et al. (2016), who both found that the CBOE was undetectable in their data sets. Those objects for which the values of B_o are ≤ 1 include Steins (Spjuth et al. 2012), Itokawa (Kitazato et al. 2008; Tatsumi et al. 2019), Eros (Clark et al. 2002; Domingue et al. 2002), Ryugu (Tatsumi et al. 2020), and the Moon (Helfenstein & Veverka 1987), and thus provide the best comparisons with this study of Ryugu. More current lunar studies by Sato et al. (2014) allow $B_o > 1$, due to studies by Hapke et al. (1993) and Muinonen et al. (2011), which suggest that coherent backscatter plays a part in the lunar opposition surge, though this contribution to the

opposition properties of the Moon has been debated (Shkuratov et al. 1999, 2012).

While it is helpful to compare the Hapke model opposition parameters of one object to another, some caveats do apply. Are the parameters derived from examining observations acquired at the same wavelength? As mentioned above, there are certain physical constraints within the regolith that must be met for the opposition to be wavelength independent. Ryugu does not meet those constraints. Did the model applied incorporate the same single-particle scattering function? Not all studies constrain the single-particle scattering properties in

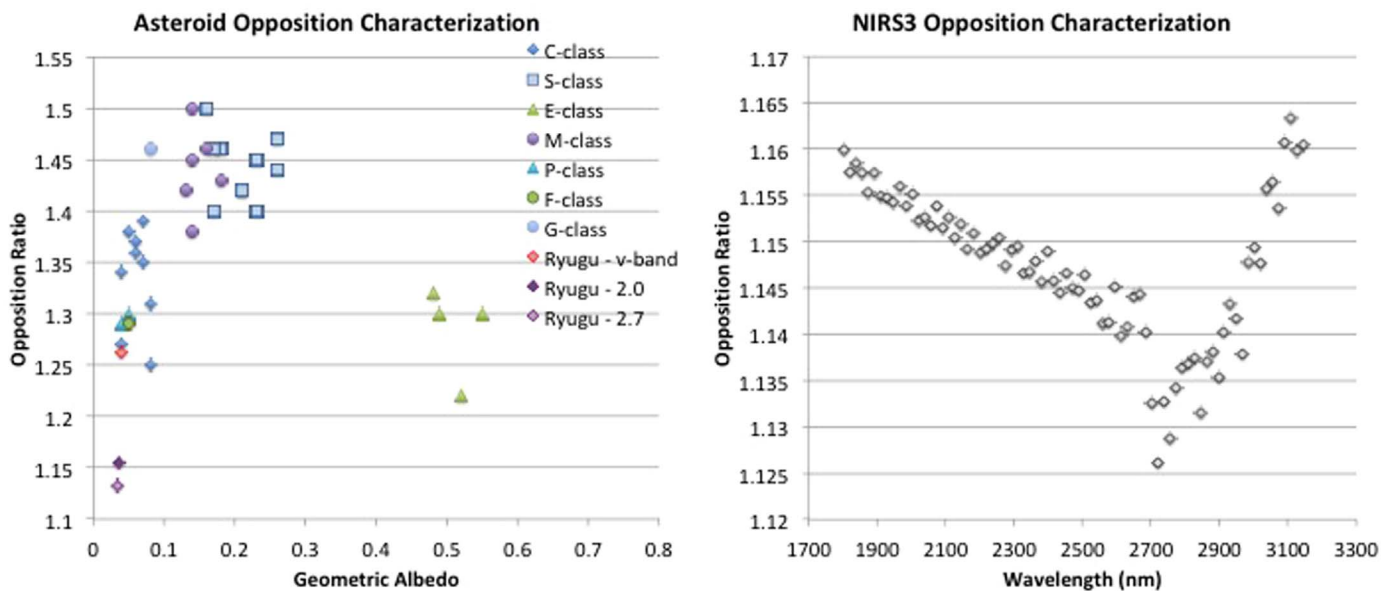


Figure 18. (Left) Comparisons of the opposition ratio (reflectance at 0.3° phase/reflectance at 5.0° phase) with the asteroid data set from Belskaya & Shevchenko (2000). (Right) Variations in the opposition ratio with wavelength at the near-infrared, as derived from the NIR3 38–40 m observations.

the same manner. The choice is often based on the phase angle coverage within the data set being modeled. For example, this study used a single-term function that allows either forward or backward scattering, but not both simultaneously. This is because the data set itself does not sample the forward scattering direction. In contrast the studies of Eros (Clark et al. 2002; Domingue et al. 2002) utilized two-term single-particle scattering functions that allow for combinations of forward and backward scattering. The single-particle scattering function can affect the reflectance observed in the opposition region ($\alpha < 5^\circ$), oftentimes in subtle ways especially if the data set is limited in geometric angle coverage.

Comparisons of Ryugu’s opposition parameter values (Figure 17) with those from studies of other solar system objects show that, in general, Ryugu’s opposition width is broader but its amplitude overlaps with the opposition characteristics of Eros, Itokawa, and some early studies of the lunar surface. The values shown for comparison are predominately from visible wavelength observations, whereas the NIR3 results are from near-infrared observations. The different wavelength regions could be a contributor to the differences seen between Ryugu and these other objects. The ONC-T visible observations for Ryugu shown (Tatsumi et al. 2020) are closer to those for the Itokawa and Helfenstein & Veverka (1987) study of the Moon. The opposition amplitude is identical between Ryugu and Itokawa in the visible. Comparisons of Ryugu in the visible and the near-infrared show the amplitude is similar but the opposition width is broader in the near-infrared.

Near-infrared modeling results for Eros (Clark et al. 2002) and Itokawa (Kitazato et al. 2008) show the same relationship with the Ryugu results as the visible wavelength studies: overlapping amplitude values and wider width values for Ryugu. One physical parameter of the regolith that could produce this difference is a higher-porosity coefficient for Ryugu compared to either Eros or Itokawa. Variations in the extinction properties, with Ryugu having either a higher extinction coefficient or extinction radius for the constituent grains in its regolith, could also explain the difference. The much darker albedo of Ryugu’s

regolith is commensurate with higher extinction coefficient or extinction radius values than those for either Eros or Itokawa.

Another method for characterizing the opposition surge is to examine and compare the reflectance at 0.3° phase with the reflectance at 5.0° phase. Belskaya & Shevchenko (2000) examine the ratio of the reflectance at these two phase angles for several asteroids observed in the visible at $0.55 \mu\text{m}$ (see Belskaya & Shevchenko 2000, Table 2). A plot of the geometric albedo versus this opposition ratio (Figure 18) is compared with values from Tatsumi et al. (2020) from the observations at $0.55 \mu\text{m}$ (v-band) and those from this study at 2.0 and $2.7 \mu\text{m}$. We used the geometric albedo at $0.55 \mu\text{m}$ derived by Tatsumi et al. (2020) of 0.04 ± 0.005 and use their Hapke parameter values to derive the reflectance of Ryugu at 0.3° and 5.0° phase to calculate the ratio. The v-band value for Ryugu plots within the grouping for C-, F-, and P-class asteroids in the ECAS taxonomy.

The near-infrared ratio values were derived from the 38–40 m data observations. All observations within $0.3^\circ \pm 0.005^\circ$ were averaged together to provide the reflectance value at 0.3° phase. All observations within $5.0^\circ \pm 0.005^\circ$ were averaged together to provide the reflectance value at 5.0° phase. The ratio was then calculated for each wavelength (Figure 18). The geometric albedos at 2.0 and $2.7 \mu\text{m}$ were derived using the Hapke model and the model parameter values for those wavelengths. The values at 2.0 and $2.7 \mu\text{m}$ are compared with the 550 nm values. The near-infrared ratios are much lower than their visible counterparts, and the geometric albedo values at $2.0 \mu\text{m}$ and $2.7 \mu\text{m}$ (0.035 and 0.033 , respectively) are significantly darker than the value at $0.55 \mu\text{m}$. The properties of Ryugu’s opposition in the near-infrared are clearly different than those for other objects observed in the visible.

The opposition ratio for Ryugu also shows a strong variation with wavelength, as is seen in the Hapke modeling results. This variation with wavelength supports the finding from the modeling that the opposition is not only dependent on the albedo of the surface but is influenced by the physical structure of the regolith.

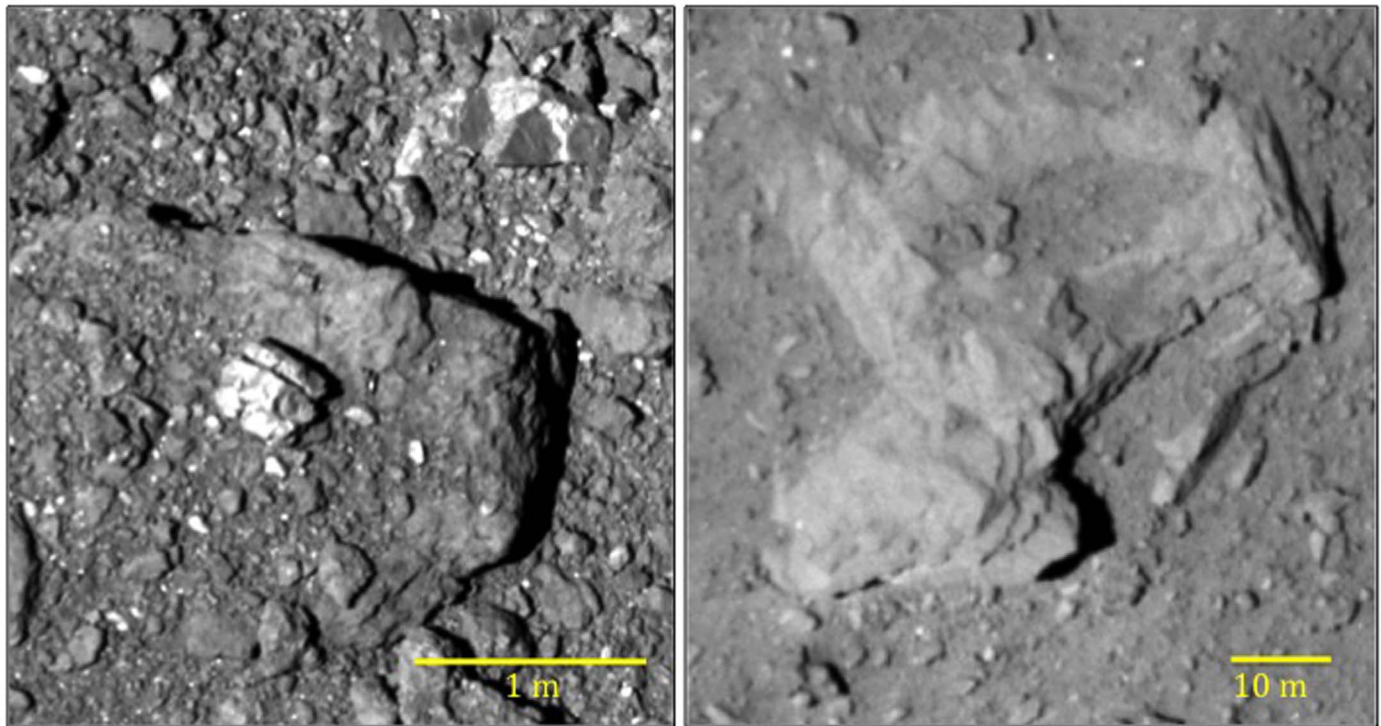


Figure 19. (Left) A boulder near the MINERVA-II landing site partially covered with regolith. (Right) Type 2 boulder displaying some coverage by regolith. Coarse-grained (millimeter to centimeter) regolith is apparent at the resolution of both these images

7. Discussion/Conclusions

This study of Ryugu's opposition surge in the near-infrared provides some additional insight into the properties of the optically active portion of its regolith. Unlike the photometric behavior observed in the visible, which shows the opposition model parameters to be uniform with wavelength (Tatsumi et al. 2020), the opposition parameters in the near-infrared show a clear variation with wavelength. The variation in both amplitude and width is commensurate with wavelength dependencies in the absorption and physical properties (particle shape and distribution of sizes) of the regolith material. While the near-infrared spectra acquired by the NIRS3 instrument display a very dark, flat spectrum with a single sharp absorption at $2.72\ \mu\text{m}$, the photometry shows broader variations in the opposition parameters, with a maximum near $2.74\ \mu\text{m}$ and $2.8\ \mu\text{m}$, for B_o and h , respectively. Based on the Hapke model derivation and definitions of the opposition parameters, the wavelength dependence of both the opposition amplitude and width is attributable to the physical properties (such as absorption properties, particle shape, and grain size distribution) of the regolith and not only the regolith's albedo. This is also supported by the opposition ratio properties.

The wavelength variation in the opposition amplitude can be ascribed to either (or both) the composition of the regolith or the nature of the scattering centers within the regolith grains. The nature of the scattering centers is to reflect the incident light such that it does not return directly to the detector and is multiply scattered such that it is lost to detection. This can be accomplished via composition (highly absorbing media), particle inclusions, or particle shape. Ryugu's dark regolith is composed of highly absorbing material, thus making it difficult to discern the role of the regolith particle characteristics solely based on the opposition amplitude.

The opposition width wavelength characteristics argue that one or more of the following characteristics are invalid for describing Ryugu's regolith: (1) regolith grains/particles are larger than the wavelength of light, (2) these grains/particles are equant, and (3) the grain/particle size distribution is narrow. ONC images of Ryugu's surface boulders (Figure 19) shown by Sugita et al. (2019) clearly show the presence of a granular component in Ryugu's surface, even though it may not completely cover the entire surface. ONC images acquired at $\sim 42\ \text{m}$ altitude show regions on the surface containing particles several centimeters in size (Sakatani et al. 2019). The MASCOT lander studies do not show any evidence for fine-grained dust (Biele et al. 2019; Grott et al. 2019; Jaumann et al. 2019). However, thermal studies suggest that the boulders on Ryugu are highly porous (Okada et al. 2020; Shimaki et al. 2020). The thermal inertia properties show that Ryugu's boulders are consistent with a fragile porous matrix that is easily disrupted to produce fine grains (Okada et al. 2020; Shimaki et al. 2020). These fine grains could accumulate on the surface to mix with the coarser-grained regolith, or even coat the coarser grains, apparent in the images. Observations of particles elevated by the thrusting during the TD1 operations (Morota et al. 2020; Tsuda et al. 2020) along with the thermal inertia measurements (Shimaki et al. 2020) suggest that fine grains exist in some regions as a portion of Ryugu's regolith. This is commensurate with the photometric behavior of the spectral slope we observe in the NIRS3 data set. The phase-reddening behavior with both phase and incidence angle, in comparison with laboratory measurements of carbonaceous meteorites, indicates a granular regolith with a fine-grained ($<45\ \mu\text{m}$) component.

In 2020 December, the samples collected from Ryugu's surface were returned to Earth. Insight into the properties of

Ryugu's regolith will be revealed in the analyses of these samples.

ORCID iDs

Deborah Domingue <https://orcid.org/0000-0002-7594-4634>
 Moe Matsuoka <https://orcid.org/0000-0003-1091-3041>
 Yasuhiro Yokota <https://orcid.org/0000-0001-9230-974X>
 Eri Tatsumi <https://orcid.org/0000-0002-6142-9842>
 Masanao Abe <https://orcid.org/0000-0003-4780-800X>
 Shuji Matsuura <https://orcid.org/0000-0002-5698-9634>
 Stefan Schröder <https://orcid.org/0000-0003-0323-8324>
 Faith Vilas <https://orcid.org/0000-0003-4723-5870>
 Rosario Brunetto <https://orcid.org/0000-0003-3001-9362>
 Lucille Le Corre <https://orcid.org/0000-0003-0349-7932>
 Nicholas Moskovitz <https://orcid.org/0000-0001-6765-6336>

References

- Barucci, M. A., Hasselmann, P. H., Fulchignoni, M., et al. 2019, *A&A*, **629**, A13
- Beck, P., Pommerol, A., Thomas, N., et al. 2012, *Icar*, **218**, 364
- Belskaya, I. N., & Shevchenko, V. G. 2000, *Icar*, **147**, 94
- Biele, J., Kührt, E., Senshu, H., et al. 2019, *PEPS*, **6**, 48
- Binzel, R. P., DeMeo, F. E., Burt, B. J., et al. 2015, *Icar*, **256**, 22
- Brunetto, R., Lantz, C., Ledu, D., et al. 2014, *Icarue*, **237**, 278
- Clark, B. E., Helfenstein, P., Bell, J. F., et al. 2002, *Icar*, **155**, 189
- Clark, B. E., Veverka, J., Helfenstein, P., et al. 1999, *Icar*, **140**, 53
- Cloutis, E. A., Hudon, P., Hiroi, T., et al. 2013, *LPSC*, **44**, 1550
- Cloutis, E. A., Hudon, P., Hiroi, T., Gaffey, M. J., & Mann, P. 2011, *Icar*, **216**, 309
- Cloutis, E. A., Pietrasz, V. B., Kiddell, C., et al. 2018, *Icar*, **305**, 203
- Dlugach, Zh. M., & Mishchenko, M. I. 2013, *SoSyR*, **47**, 454
- Domingue, D., Palmer, E., Gaskell, R., & Staid, M. 2018, *Icar*, **312**, 61
- Domingue, D., Robinson, M., Carcich, B., et al. 2002, *Icar*, **155**, 205
- Domingue, D. L., Denevi, B. W., Murchie, S. L., & Hash, C. D. 2016a, *Icar*, **268**, 172
- Domingue, D. L., Murchie, S. L., Denevi, B. W., Ernst, C. M., & Chabot, N. L. 2015, *Icar*, **257**, 477
- Domingue, D. L., Vilas, F., Choo, T., et al. 2016b, *Icar*, **280**, 340
- Feller, C., Fornasier, S., Hasselmann, P. H., et al. 2016, *MNRAS*, **462**, S287
- Fornasier, S., Hasselmann, P. H., Barucci, M. A., et al. 2015, *A&A*, **583**, A30
- Gillis-Davis, J. J., Lucey, P. G., Bradley, J. P., et al. 2017, *Icar*, **286**, 1
- Gillis-Davis, J. J., Lucey, P. G., Bradley, J. P., Ishii, H. A., & Connolly, H. C. 2013, *LPSC*, **44**, 2494
- Gradie, J., & Veverka, J. 1986, *Icar*, **66**, 455
- Gradie, J., Veverka, J., & Buratti, B. 1980, *LPSC*, **11**, 357
- Grott, M., Knollenberg, J., Hamm, M., et al. 2019, *NatAs*, **3**, 971
- Hapke, B. 1981, *JGR*, **68**, 4571
- Hapke, B. 1984, *Icar*, **59**, 41
- Hapke, B. 1986, *Icar*, **67**, 264
- Hapke, B. 1993, *Theory of Reflectance and Emittance Spectroscopy* (Cambridge: Cambridge Univ. Press)
- Hapke, B. 2002, *Icar*, **157**, 523
- Hapke, B. 2008, *Icar*, **195**, 918
- Hapke, B. 2012, *Theory of Reflectance and Emittance Spectroscopy* (2nd ed; New York: Cambridge Univ. Press)
- Hapke, B. W., Nelson, R. M., & Smythe, W. D. 1993, *Sci*, **260**, 509
- Hasselmann, P. H., Barucci, M. A., Fornasier, S., et al. 2016, *Icar*, **267**, 135
- Hasselmann, P. H., Barucci, M. A., Fornasier, S., et al. 2017, *MNRAS*, **S550**
- Helfenstein, P., & Shepard, M. K. 2011, *Icar*, **215**, 83
- Helfenstein, P., & Veverka, J. 1987, *Icar*, **72**, 342
- Helfenstein, P., Veverka, J., Thomas, P. C., et al. 1994, *Icar*, **107**, 37
- Helfenstein, P., Veverka, J., Thomas, P. C., et al. 1996, *Icar*, **120**, 48
- Hiroi, T., Pieters, C. M., Zolensky, M. E., & Lipschutz, M. E. 1993, *Sci*, **261**, 1016
- Hiroi, T., Sasaki, S., Misu, T., & Nakamura, T. 2013, *LPSC*, **44**, 1276
- Iwata, T., Kitazato, K., Abe, M., et al. 2017, *SSRv*, **208**, 317
- Jaumann, R., Schmitz, N., Ho, T.-M., et al. 2019, *Sci*, **365**, 817
- Johnson, T. V., & Fanale, F. P. 1973, *JGR*, **78**, 8507
- Kaydash, V., Korokhin, V., Velikodsky, Y., et al. 2012, *JQSRT*, **113**, 2431
- Kitazato, K., Clark, B. E., Abe, M., et al. 2008, *Icar*, **194**, 137
- Kitazato, K., Milliken, R. E., Iwata, T., et al. 2019, *Sci*, **364**, 272
- Lantz, C., Brunetto, R., Barucci, M. A., et al. 2015, *A&A*, **577**, A41
- Lantz, C., Brunetto, R., Barucci, M. A., et al. 2017, *Icar*, **285**, 43
- Lantz, C., Clark, B. E., Barucci, M. A., & Lauretta, D. S. 2013, *A&A*, **554**, A138
- Lazzarin, M., Marchi, S., Moroz, L. V., et al. 2006, *ApJ*, **647**, L179
- Le Corre, L., Sanchez, J. A., Reddy, V., et al. 2017, *MNRAS*, **475**, 614
- Lederer, S. L., Domingue, D. L., Thomas-Osip, J. E., et al. 2008, *EP&S*, **60**, 49
- Li, J., A'Hearn, M. F., & McFadden, L. A. 2004, *Icar*, **172**, 415
- Markkanen, J., Agarwal, J., Väisänen, T., Penttilä, A., & Muinonen, K. 2018, *ApJL*, **868**, L16
- Li, J. Y., Le Corre, L., Schröder, S. E., et al. 2013, *Icar*, **226**, 1252
- Masoumzadeh, N., Boehnhardt, H., Li, J.-Y., & Vincent, J.-B. 2015, *Icar*, **257**, 239
- Matsuoka, M., Nakamura, T., Hiroi, T., Okumura, S., & Sasaki, S. 2020, *ApJL*, **890**, L23
- Matsuoka, M., Nakamura, T., Kimura, Y., et al. 2015, *Icar*, **254**, 135
- Mishchenko, M. I., Dlugach, J. M., Lui, L., et al. 2009, *ApJL*, **705**, L118
- Mishchenko, M. I., & Dlugach, J. M. 1993, *P&SS*, **41**, 173
- Morota, T., Sugita, S., Cho, Y., et al. 2020, *Sci*, **368**, 654
- Moroz, L. V., Hiroi, T., Shingareva, T. V., et al. 2004, *LPSC*, **35**, 1279
- Moskovitz, N. A., Abe, S., Pan, K.-S., et al. 2013, *Icar*, **224**, 24
- Muinonen, K., Parviainen, H., Naranen, J., et al. 2011, *A&A*, **531**, A150
- Nakamura, T., Lantz, C., Nakauchi, Y., et al. 2020, *LPSC*, **51**, 1310
- Nesvorný, D., Jedicke, R., Whiteley, R. J., & Ivezić, Z. 2005, *Icar*, **173**, 132
- Okada, T., Fukuhara, T., Tanaka, S., et al. 2020, *Natur*, **579**, 518
- Pilorget, C., Fernando, J., Riu, L., Kitazato, K., & Iwata, T. 2021, *Icar*, **355**, 114126
- Potin, S., Beck, P., Schmitt, B., & Moynier, F. 2019, *Icar*, **333**, 415
- Sakatani, N., Sugita, S., Honda, R., et al. 2019, *LPSC*, **50**, 1732
- Sato, H., Robinson, M. S., Hapke, B., Denevi, B. W., & Boyd, A. K. 2014, *JGRE*, **119**, 1775
- Shevchenko, V. G., Chiorny, V. G., Gaftonyuk, N. M., et al. 2008, *Icar*, **196**, 601
- Schröder, S. E., Li, J.-Y., Rayman, M. D., et al. 2018, *A&A*, **620**, A201
- Schröder, S. E., Mottola, S., Keller, H. U., Raymond, C. A., & Russell, C. T. 2014, *P&SS*, **103**, 66
- Shepard, M. K., & Helfenstein, P. 2007, *JGRE*, **112**, E03001
- Shevchenko, V. G., & Belskaya, I. N. 2010, *European Planetary Science Congress 2010*, 738
- Shevchenko, V. G., Belskaya, I. N., Slyusarev, I. G., et al. 2012, *Icar*, **217**, 202
- Shimaki, Y., Senshu, H., Sakatani, N., et al. 2020, *Icar*, **348**, 113835
- Shkuratov, Y. G., & Helfenstein, P. 2001, *Icar*, **152**, 96
- Shkuratov, Y., Kaydash, V., Korokhin, V., et al. 2012, *JQSRT*, **113**, 2431
- Shkuratov, Y. G., Kreslavsky, M. A., Ovcharenko, A. A., et al. 1999, *Icar*, **141**, 132
- Shkuratov, Y. G., Starukhina, L. V., Kreslavsky, M. A., et al. 1994, *Icar*, **109**, 168
- Sierks, H., Barbieri, C., Lamy, P. L., et al. 2015, *Sci*, **347**, aaa1044
- Souchon, A. L., Pinet, P. C., Chevrel, S. D., et al. 2011, *Icar*, **215**, 313
- Spjuth, S., Jorda, L., Lamy, P. L., Keller, H. U., & Li, J.-Y. 2012, *Icar*, **221**, 1101
- Sugita, S., Honda, R., Morota, T., et al. 2019, *Sci*, **252**, 252
- Tatsumi, E., Domingue, D., Hirata, N., et al. 2018, *Icar*, **311**, 175
- Tatsumi, E., Domingue, D., Yokota, Y., et al. 2020, *A&A*, **639**, A83
- Tatsumi, E., Kouyama, T., Suzuki, H., et al. 2019, *Icar*, **325**, 153
- Thompson, M. S., Loeffler, M. J., Morris, R. V., Keller, L. P., & Christoffersen, R. 2019, *Icar*, **319**, 499
- Thompson, M. S., Morris, R. V., Clemett, S. J., et al. 2020, *Icar*, **346**, 113775
- Tsuda, Y., Saiki, T., Terui, F., et al. (Hayabusa2 Project Team) 2020, *AcAau*, **171**, 42
- Vernazza, P., Fulvio, D., Brunetto, R., et al. 2013, *Icar*, **225**, 517
- Yokota, Y., Honda, R., Tatsumi, E., et al. 2021, *PSJ*, **2**, 177